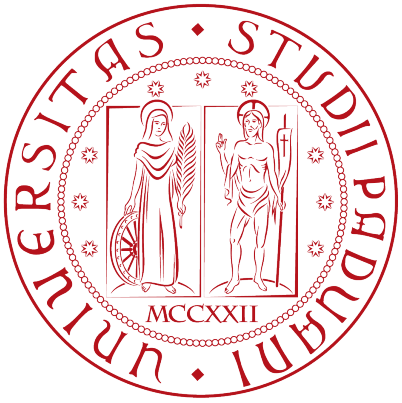

UNIVERSITÀ DEGLI STUDI DI PADOVA

Dipartimento di Fisica e Astronomia "Galileo Galilei"
Corso di Laurea Triennale in Fisica

Tesi di Laurea

Sviluppo di look-up tables nella simulazione di PeV showers per SWGO

Look-up tables for efficient simulation of PeV showers for SWGO

Relatore

Prof. Michele Doro

Laureanda

Marinella Visentini

ANNO ACCADEMICO 2022/2023

Contents

L'ampio spettro dei raggi cosmici (CRs), particelle cariche con velocità relativistiche che permeano l'Universo e raggiungono la Terra, è considerato di origine galattica fino ad energie di 3 PeV. Le sorgenti capaci di accelerare i raggi cosmici, raggiungendo energie di 10^{15} eV, rappresentano i più potenti acceleratori astrofisici di particelle all'interno della nostra galassia. Per descrivere tali oggetti è stato coniato il termine *PeVatrons*. Nonostante siano stati considerati molteplici possibili candidati (come PWNs, SNRs o superbubbles), i rivelatori di raggi γ attualmente in funzione non permettono di trarre conclusioni stringenti circa l'identità di tali acceleratori.
Il Southern Wide-field Gamma-ray Observatory (SWGO), nella cordigliera delle Ande, sarà il primo extensive air-shower array per la rivelazione di raggi γ nell'emisfero australe, garantendo l'osservazione del Centro Galattico. Uno dei principali obiettivi previsti per il nuovo ground-based detector è il raggiungimento di un'elevata sensibilità nella rivelazione in un esteso range energetico, anche oltre i 100 TeV, consentendo quindi lo studio dei PeVatrons. L'osservatorio sarà costituito da un array di Water Cherenkov Detectors (WCD), per la rivelazione della radiazione Cherenkov emessa quando le particelle delle air-showers, generate da CRs o da raggi γ, attraversano l'acqua delle tanks. SWGO si trova ancora in una fase di progettazione, per scegliere al meglio il sito, la tipologia di detector unit, e il layout dell'array. Questa tesi si propone di contribuire ad un progetto più ampio, focalizzato sull'analisi della risposta del detector a showers di particelle al PeV. Tale studio verrà portato avanti attraverso lo sviluppo di una simulazione parametrizzata e più efficiente della risposta del rivelatore, mediante la creazione di Look-Up Tables. L'analisi proposta in questa tesi si focalizza sullo studio della risposta di una specifica tipologia di detector unit (la tank A, a due livelli), attraverso la simulazione ripetuta di single-particle hits. L'interazione viene analizzata considerando il numero di fotoelettroni generati nei PMT (distinguendo il PMT dello strato superiore da quello inferiore) e osservandone l'andamento in funzione della natura della particella (elettroni, muoni), dell'energia e della configurazione geometrica di incidenza.

The extensive spectrum of cosmic rays, relativistic charged particles that permeate the universe and reach the Earth, is associated to Galactic origins up to 3 PeV. Their sources, able to accelerate particles up to 10^{15} eV, represent the most powerful astrophysical particle accelerators within our Galaxy. The term *PeVatrons* was coined to describe these objects. While various candidates are being considered (such as PWNs, SNRs or superbubbles), strong constraints on these accelerators identities are almost impossible with current γ-ray instruments.
The Souther Wide-field Gamma-ray Observatory (SWGO), located in the Andean Mountains, will be the first extensive air-shower array for γ-ray detection in the Southern Hemisphere, providing access to the Galactic Center. Its primary objective is to achieve high sensitivity across a wide energy range, extending beyond a 100 TeV high-energy threshold, thus enabling the detection of PeVatrons. The observatory will consist of Water Cherenkov Detector units (WCD), designed to measure the Cherenkov light emitted when particles from atmospheric showers, generated by cosmic rays or γ-rays, cross the water tanks. SWGO is still in a design phase investigating the optimal location, configuration of detector units, and array layout. The study proposed in this thesis is part of a larger project, analyzing the response of the detector to PeV atmospheric showers. This is achieved by developing a more efficient parameterized simulation of the detector response, through the creation of Look-Up Tables. This thesis is focused on analyzing the response of a specific detector unit design (tank A, a dual-layer unit), through repeated single-particle hit simulations. It studies how the number of photo-electrons generated in the PMTs (distinguishing between the PMT in the upper and lower volume) varies in response to several factors. These factors include the type of particle (muons and electrons), the particle's energy, and the specific geometric configuration of the hit.

1. Introduction

Cosmic rays (CRs) and γ-rays

The term *cosmic-rays* (CRs) is used to collectively refer to a set of relativistic charged particles, consisting of approximately 92% protons, 6% Helium, 1% electrons, 1% heavier nuclei [Cri21] and an unprecised ammount of neutrinos. These particles permeate our Galaxy, as well as the extragalactic space, and reach the Earth, constantly interacting with its atmosphere.

The discovery of CRs dates back to 1912, through the balloon observations conducted by the Austrian physicist Victor Hess [DP18]). However, the fundamental question regarding their origin remains unanswered.

Their energy spectrum, represented in Figure 1.1, spans an extensive range, from 10^9 to 10^{21} eV. At energies below 100 GeV they are absorbed due to the interaction with the solar wind [Kac08]). Historically, their spectrum has been described by a power-law function $I(E) \sim E^{-\alpha}$ and divided in subregions associated with different sources (with the sprectral index α changing between regions). CRs with energies up to 3 PeV ($3 \cdot 10^{15}$ eV, known as the *knee*) are believed to be accelerated within our galaxy (Galactic CRs) and they exhibit a power-law of spectrum $\propto E^{-2.7}$. Beyond the knee, the slope changes to $\propto E^{-3.1}$ up to the so called *ankle* region (at $3 \cdot 10^{18}$ eV) where the spectrum hardens back to $\alpha = -2.7$, due to the contribution of an extragalactic component [CG23].

Therefore, the sources responsible for Galactic cosmic rays must be able to accelerate particles up to PeV energies. To identify these objects, that constitute the most powerful astrophysical particle accelerators, the term *PeVatron* was coined.

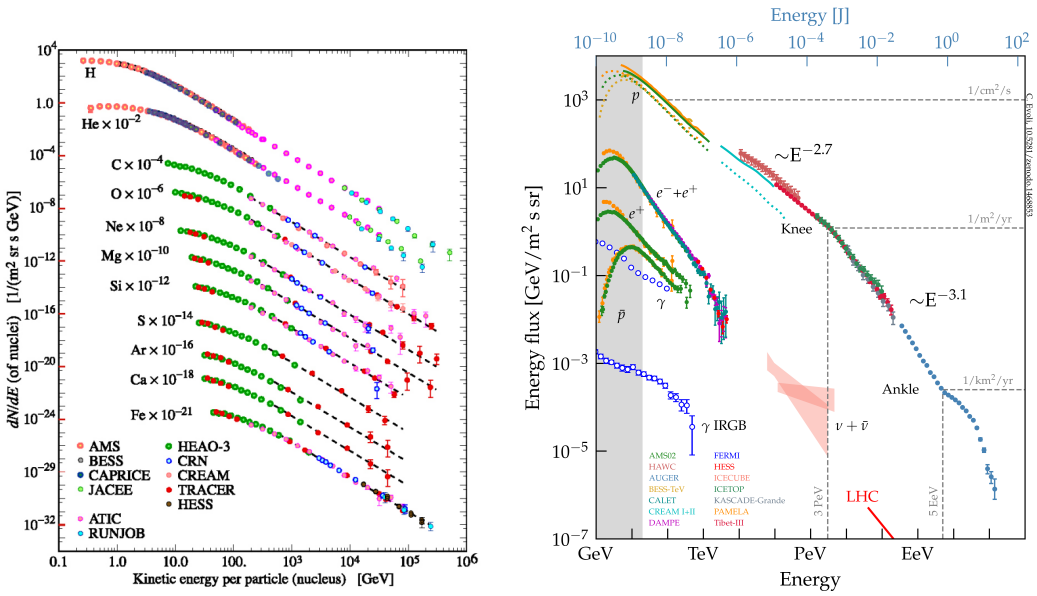

Figure 1.1: Differential energy spectrum and particle composition of CRs.

Cosmic-rays acceleration and their propagation are both linked to γ-rays emission. CRs, as charged particles, are deflected by cosmic magnetic fields, losing the information on their place of production (they arrive almost isotrop-

ically to the Earth). On the other hand there is no physical mechanism to deflect γ-rays so they travel undisturbed. However γ-rays are much less frequent that CRs: approximately one γ-ray is observed every 1000 CRs at TeV energies [Dor09].

As previously mentioned, high-energy CRs interact with matter, photon and magnetic fields while propagating, in processes that lead to the emission of γ-rays. When cosmic rays encounter dense regions of the Interstellar Medium (ISM), they can engage in *leptonic emission-mechanisms*. For instance, Bremsstrahlung radiation is produced when electrons interact with the electromagnetic field of the nuclei ($e^-(\gamma) \rightarrow e^- \gamma$). If these electrons achieve energies in the TeV range or beyond, emission of γ-rays is observed. Electrons can also interact with low-energy positron fields and annihilate producing two energetic photons ($e^+ e^- \rightarrow \gamma \gamma$). Interaction with matter also plays a role in *hadronic emission-mechanisms*. The inelastic collision between accelerated hadrons and ISM nuclei generates pions (π^+, π^-, π_0). Charged pions decay emitting neutrinos while neutral pions annihilate into two energetic gammas ($\pi^0 \rightarrow \gamma \gamma$). Dense low-energy photon fields are related to another *leptonic mechanism*, the Inverse Compton scattering. This process involves high-energy electrons interacting with low energy photons (CMB, optical, infrared). The momentum transferred from the electron to the photon causes it to be re-emitted at much higher energies ($\gamma e \rightarrow \gamma e$). In regions with dense radiation fields, Hadronic Inverse Compton scattering could also occur. One last channel of γ-ray production worth mentioning is the synchrotron emission from TeV electrons or super-PeV protons in the presence of local strong magnetic fields. [LL92]

In the TeV domain, it's hard to differentiate between these potential sources and to know if hadrons or leptons are responsable for the γ-ray production because the resulting γ-ray spectrum is similar. However, cosmic rays primarily consist of protons. Therefore, when seeking the origin of cosmic rays, it's interesting to focus on proton sources. It's important to note that an efficient electron accelerator might not necessarily be an efficient proton accelerator [Cri21]).

Until recently, a detection of UHE γ-ray photons (Ultra High Energy, $E > 100 TeV$) was considered evidence of accelerated CRs as it was claimed that above 50 TeV electron IC scattering becomes inefficient (due to the Klein-Nishina suppression). The detection of neutrinos would also be an effective way to discriminate between these mechanisms, as they are produced dominantly through hadronic interactions. Another direct proof of energized CRs could be represented by the detection of the *pion-bump*, which is related to the energy corresponding to the rest mass of π_0 (around 100 MeV) [CG23].

Pevatron candidates

The recent detection of 12 UHE γ-ray Galactic sources, with energies beyond 100 TeV, by the LHAASO observatory, has marked a significant breakthrough in the CRs origin search [CG23]. Which astrophysical sources can energize cosmic-rays up to PeV energies? It's crucial to point out that the ability to accelerate particles up to PeV energies is a necessary condition that these candidate sources must exhibit, but is not sufficient [Cri21]. This is exemplified by the case of the *Pulsar Wind Nebula* known as the *Crab Nebula*.

At the end of the life of stars with masses greater than 5 - 8 $M_\odot$, when no nuclear process is left to release energy, a dramatic collapse occurs and all the matter is converted into neutrons via inverse β-decay. As the density reaches nuclear values, the resulting neutron star begins to rotate rapidly, with periods on the order of ms, becoming a

pulsar. The pulsar expells a relativistic wind of particles and magnetic fields which generate a synchrotron nebula in the sorroundings, known as *Pulsar Wind Nebula (PWN)* [Dor09]. The best known object belonging to this category is the *Crab Nebula* (captured in Figure 1.2), related to the first observation of VHE γ-ray emission from an astrophysical source, in 1989 [Cri21].
Extensive observations, confirmed by the recent detection of gamma-rays above 1 PeV from the LHAASO collaboration, led to the conclusion that an *electron pevatron* is located within the Crab Nebulae (its synchrotron spectrum consitutes a direct proof that electron acceleration is taking place). The UHE γ-ray detection from this source pointed out that leptons are able to emit beyond the Klein-Nishina limit cited before [CG23]. Hence, despite its Pevatron nature, the Crab Nebula cannot be regarded as one of the primary CRs sources. The very low angular resolution of the LHAASO detector makes it difficult to spatially resolve the sources and to specify which astrophysical objects are responsible for the emissions.
Nonetheless, it appears that also over 30% of the detected candidate PeVatrons are potentially linked to PWNe and other leptonic accelerators. This could be due to a statistica bias, as PWNe are the most numerous γ-ray sources in our Galaxy [CG23].

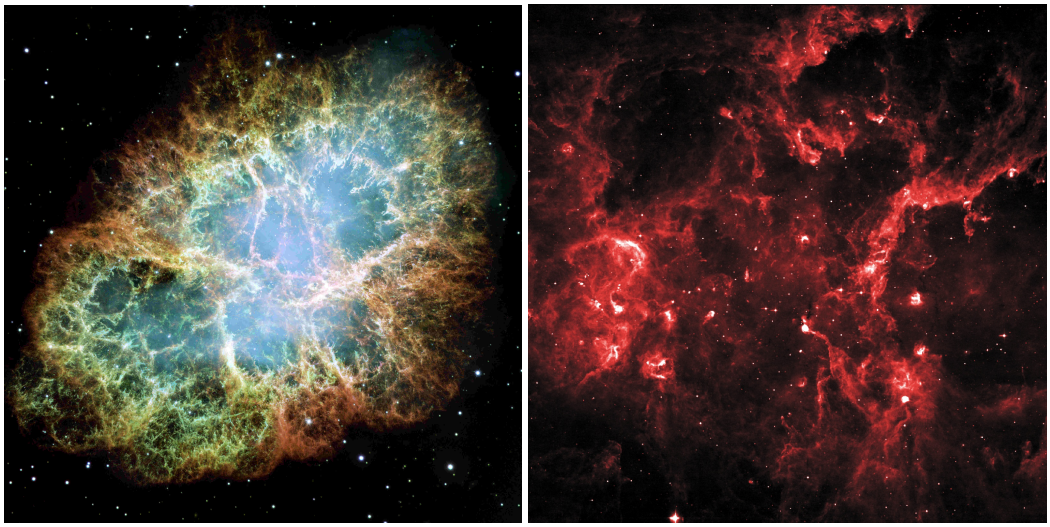

Figure 1.2: *(left)* Picture of the Crab nebula captured by the Hubble telescope. *(right)* Infrared image of the Cygnus region (Credits: NASA/IPAC/MSX).

The astrophysical objects most often cited as candidates for the origin of CRs are the *Supernova Remnants (SNRs)*. Those sources are generated during the dramatic collapse of massive stars. In the same process described before talking about PWNe origin, when the density of the neutron star reaches nuclear values no further compression is possible. As a result, half of the mass is ejected outwards forming a propagating nebula called *Supernova Remnant*. SNRs represent the ideal laboratories for particle acceleration through the *DSA (Diffusive Shock Acceleration) mechanism*, theorized by Fermi. As the nebula propagates, a shock wave is formed at the head of the shell. This shock interacts with local gas fields, accelerating particles with an average energy gain of $\overline{\varepsilon} \sim \frac{4}{3}\beta$ (where β is the relative velocity of the CRs-particles). [Kac08]

It has been proven that SNRs are capable of accelerating CRs of low energy (E < 100GeV). In fact, observations of the SNR W44 by the AGILE and Fermi-LAT satellites in 2011 revealed a spectrum exhibiting a clear correlation with the presence of the pion-bump. However, no SNR has been detected yet emitting gamma-rays at energies exceeding 100 TeV (the energy of γ-rays produced from accelerated protons scales as $E_\gamma \propto 1/10E_p$, so the detection of 100 TeV γ-rays probes the acceleration of PeV CR protons). One potential theoretical explanation could be that only a small fraction of SNRs are PeVatrons (generated from peculiar Supernovae, sufficiently energetic or exploding in dense winds) and that the duration of the PeVatron phase is rather limited [Cri21]. They could be able to accelerate CRs at these energies only in the first 100 years of their life and all the known SNRs are older [CG23]. However LHAASO results show that half of its 12 PeVatrons could be still associated to middle-aged SNRs, but strong constraints on the sources (except for the Crab Nebula) are impossible with the current instruments [CG23]. Potential alternative sources have also been considered, including clusters of massive stars and superbubbles (giant cavities of plasma inflated by repeated SNe explosions). The γ-ray emission observed by the Fermi-LAT satellite from the superbubble located in the Cygnus region (captured in Figure 1.2), coupled with the detection of high-energy neutrinos, has been claimed as a clear evidence of PeV protons acceleration [Cri21]. LHAASO collaboration has also reported the detection of γ-rays with energies beyond 1 PeV from a couple of sources, including the Crab Nebula. If these emissions result from hadronic interactions, it could suggest the presence of Galactis SuperPeVatrons [Cri21]. Many aspects of astrophysical acceleration of PeV particles are still unknown. In order to move forward it's important the progress on the spatial, time and spectral resolution of γ-ray observations (the angular resolution and sensitivity of the existing UHE instruments are represented in Figure 1.3).
However, with only 10 months of observations, LHAASO tripled the number of known sources emitting above 100 TeV, proving that this feature is quite common on galactic sources [CG23].

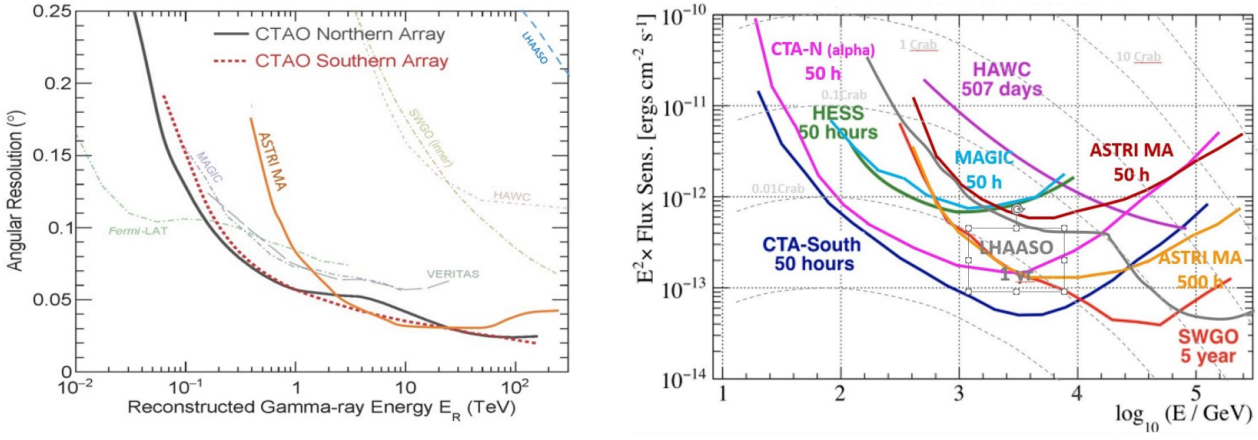

Figure 1.3: Angular resolution (*left*) and differential sensitivity curves (*right*) of current and future VHE/UHE instruments [CG23].

Atmospheric showers

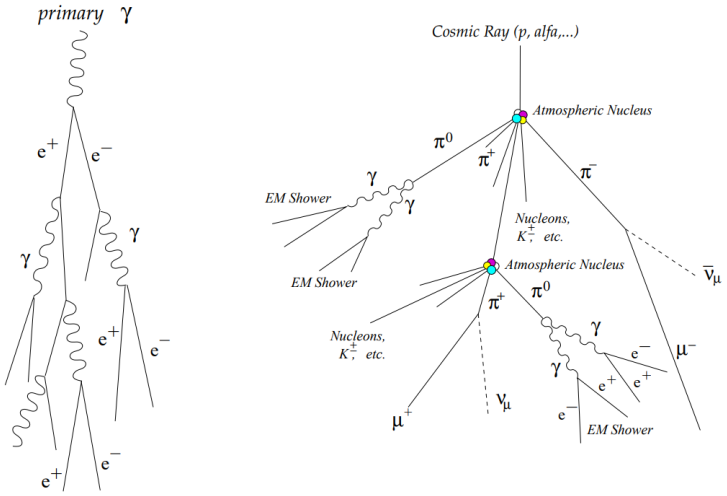

Figure 1.4: Scheme of production of an electromagnetic (*left*) and an hadronic shower (*right*) [Dor09].

When CRs and γ-rays reach the Earth, they interact with the atmosphere producing showers of particles. These cascades are highly valuable for their indirect detection. The composition and structure of these atmospheric showers vary based on whether they are initiated by γ-rays or hadrons, as illustrated in the graphical scheme in Figure 1.4.

- *Electromagnetic shower:*
  In such a cascade only EM interactions come into play. The primary γ-ray interacts with the electric field of atmospheric molecules and generates an $e^- - e^+$ couple through pair-production (the cross section for $\mu^- - \mu^+$ pair-production is considerably smaller by many orders of magnitude, therefore this interaction only becomes relevant for primary particles with PeV energies). Each subsequent $e^- - e^+$ generates new γ-rays via Bremsstrahlung. These secondary γ-rays carry away approximately half of the particle's energy and again pair-produce an $e^- - e^+$ couple, and so on. The process ceases when the $e^\pm$ mean energy drops below the critical energy threshold for Bremsstrhalung and the pair-production cross-section is no longer dominant. An EM shower is strongly collimated along the incident direction. [RG41]

- *Hadronic shower:*
  The shower is initiated with the production of pions, kaons and nuclons due to the strong interaction of the hadrons with atmospheric nuclei. Subsequently, charged pions and kaons decay into muons and neutrinos ($\pi^\pm \to \mu^\pm + \nu_\mu(\overline{\nu_\mu})$; $K^\pm \to \mu^\pm + \nu_\mu(\overline{\nu_\mu})$; $K^\pm \to \pi^\pm + \pi^0$), while neutral pions generate two γ-photons ($\pi_0 \to \gamma\gamma$). The process ends when the mean energy per particle falls below the pion production threshold (around 1 GeV). As a result, hadron-induced showers exhibit three main components: an hadronic core of high energy nucleons and mesons; a muonic component that, due to its large lifetime, can travel through a relevant portion of the atmosphere carring away a substantial part of the initial hardon energy; an electromag-

netic component, that counts for about one thid of the energy and produce EM sub-showers. In the hadronic cascades the heavy particles, with their large momenta, spread the shower width. [RG41]

The Souther Wide-field Gamma-ray Observatory (SWGO)

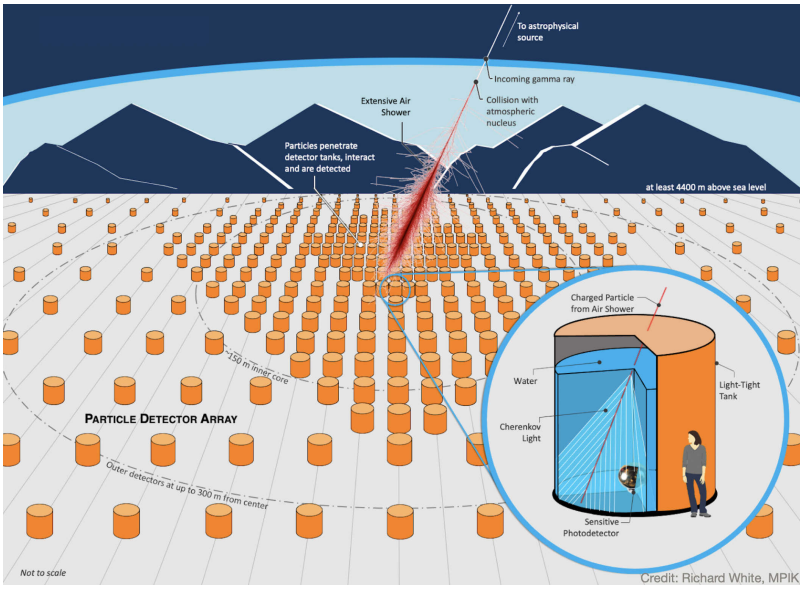

Figure 1.5: Representation of the SWGO observatory [SWG22].

The direct detection of astrophysical γ-rays is only possible through satellite-based detectors. An alternative approach is to resort to the atmospheric showers that they generate, for indirect detection. These cascades can be studied using two complementary types of observatories: Imaging Atmospheric Cherenkov Telescopes (IACTs) (highly sensitive, but with a narrow filed-of-view) and Extensive Air-Shower arrays (EASs) [Alm21].

The Souther Wide-field Gamma-ray Observatory (SWGO) will be the first extensive air-shower array for γ-ray detection in the Southern Hemisphere. It's intended to be a southern version of the existing ground-base detector arrays, HAWC, in Mexico, and LHAASO, in China. [SWG22] The observatory will be composed of Water Cherenkov Detector units (WCD) equipped with photomultipliers, to sample the atmospheric showers by measuring the Cherenkov light emitted when the shower particles cross the water tanks, as illustrated in the graphical scheme in Figure 1.5 .

The new observatory is planned to be situated in the Andean Mountains, at an altitude of 4.4km a.s.l or above. This location is favorable for two primary reasons: it provides the opportunity to access to the Galactic Centre (not accessible from HAWC and LHAASO sites), in complementarity with CTA-South (Cherenkov Telescope Array), and also enables to achieve a lower energy threshold for detected signals.

The goal is to reach a good sensitivity over an extended energy range, spanning from 100 GeV to beyond 100 TeV. The array layout is made of several circular zones, 2 or 3, of different unit density, with a gradient form a high fill factor in the inner array towards lower fill factors in the outer zones. The baseline design consists of a combination of a high fill-factor inner core of 80.000 m^2 (with a 80% fill factor), optimized for the detection of low-energy

events, and a significantly larger and sparse outer array of at least 200.000 m^2 (with a 5% fill factor), to achieve good sensitivity at 100 TeV.

A variety of Water Cherenkov Detector units are under consideration, including solutions based on tanks, ponds or for installation directly in a natural lake. These units are envisioned to be equipped with muon-tagging capability, enabling the measurement of both the electronic and muonic components of the air shower, to differentiate between an electromagnetic or an hadronic origin.

All these features are intrinsically linked to the primary scientific goals of the new observatory. These include the search for galactic particle accelerators (in particular the search for PeVatrons), as well as cosmic ray composition and anisotropy studies, and observations to constrain the nature of Dark Matter. SWGO could also play a key role in the observation of transient phenomena (thanks to the low-energy threshold, wide field of view and continuous observational duty-cycle), at the heart of multi-messanger astrophysics, as potentiam EM counterparts to neutrino and gravitational wave detections. [Alm21]

2. Methodology

SWGO is still in a design phase, investigating the location of the observatory, as well as the configuration of the detector units and the array layout to be selected.
This thesis is part of a larger work, analyzing the response of the detector to PeV atmospheric showers. The first approach to this task was to process a CORSIKA [1] cascade simulation through the software HAWCSim. HAWCsim is a GEANT4 based software that simulates the detector array and produces an output file describing the observatory's response to incoming particles interacting with the tanks. However at these high energies HAWCsim requires a cumbersome amount of time to simulate the detection of a shower, due to the extensive number of particle tracks that must be traced. In fact the standard procedure consists of tracking every single particle in the water, recording every response from each PMT in all the tanks.
It was therefore decided to look for a faster parameterized simulation of the detector response. To achieve this goal, the first step was to select the particles interacting with the array tanks from the CORSIKA simulation, using a Python mask, and to study the properties of these particles, such as their energy distribution [Lui23]. These informations could then be used to create a Look-Up Table (LUT) [2] of the detector response. The idea is to consider a grid of points sampling the possible spatial and energetic configurations of a single-particle hit, and to study the response of the detector units in each case, through repeated HAWCsim simulations. In this way it would be possible to associate an average value of the output parameters, or a statistical distribution, to all the points. When a generic particle hits a tank, an interpolator could associate its configuration to the closer point of the grid, and the Look-Up Table could directly map the event to an output (returning the average parameters, or randomly extracting them from the specific distribution) without the need to run a complete HAWCsim simulation.
This thesis work is focused on analyzing the response of a specific detector unit design.
Currently 6 different tank designs are considered (represented in Figure 2.1), with features reported in Table 2.1.

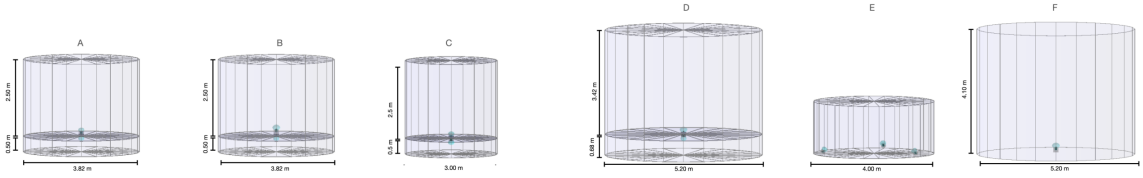

Figure 2.1: Configurations for the different WCD unit designs.

All the units are simulated using white reflective walls (made of tyvek), with the exception of the ceiling and floor of the top compartment of units A, B, C, D and F (made of polypropylene). The purpose of making these surfaces non-reflective is to minimize excessive Cherenkov light scattering, to preserve the information about the temporal development of the hits.

[1] CORSIKA is a Monte Carlo based software used to simulate the atmospheric showers.
[2] A Look-Up Table is an array storing information to replace runtime operations, directly mapping an input to an output

Label	*Layers*	*PMT (upper + lower)*	*Radius (cm)*	*Height (cm) (upper)*	*Height (cm) (lower)*
A	**2**	**8" HQE + 8"**	**191**	**250**	**50**
B	2	10" HQE + 8"	191	250	50
C	2	8" + 8"	150	250	50
D	2	10" HQE + 8"	260	342	68
E	1	3 x 8"	200	170	-
F	1	10" HQE	260	420	-

Table 2.1: Summary of the detector unit designs.

This thesis addresses the analysis of tank design A, the reference design for the dual-layer cylindrical unit. It's a cylindrical tank, with a diameter of 3.82 m and a total height of 3 m, divided into an upper layer with an height of 2.5 m and a lower one occupying the remaining height of 0.5 m. Each volume contains a photomultiplier tube (PMT) able to collect the Cherenkov light produced by the particles in the tank and to transform it into an electric signal.

The choice of a double-layer configuration was made to enhance the distinction between electromagnetic and hadronic showers. This arrangement was envisioned to provide each unit with muon-tagging capability, as they are primarily produced in hadronic cascades. Muons, highly penetrating particles, should produce a signal in both layers of the tank, while electrons should leave a trace only in the upper volume. Consequently, a signal detected in the lower layer should reveal the passage of a muon. As will be discussed later on, this discrimination process is found to be effective only for electrons below a certain energy threshold.

This analysis results are obtained through repeated `HAWCsim` simulations of a single-particle hit, focusing on one detector unit and on particles reaching the tank through its upper surface (represented in Figure 2.2). The variables taken into account in this process include the particle type, its energy, and the spatial configuration of the hit.

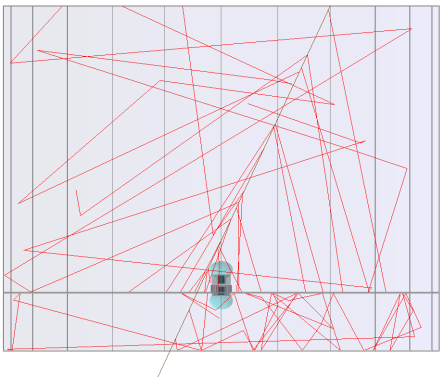

Figure 2.2: `HAWCsim` simulation for a 10 GeV muon (configuration $p_{10} - \theta_{25^\circ} - \phi_{180^\circ}$).

The simulation is run 100 times for each set of input parameters, and the position and direction of the hit are defined based on three distinct quantities (as illustrated in the graphical scheme in Figure 2.3):

- the position x, representing the radial distance from the cylinder axis;
- the zenithal angle θ, measuring the deviation of the incident direction from the vertical axis ($\theta = 0^\circ$ corresponds to a vertical hit);

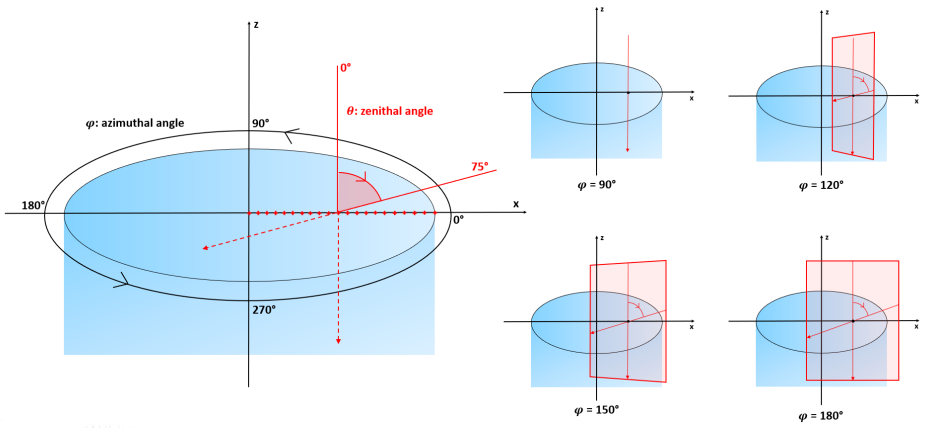

Figure 2.3: Graphical schemes referred to the definitions of the angles.

- the azimuthal angle ϕ, expressing the the rotation of the incidence plane ($\phi = 180°$ denotes a particle moving in the PMT direction).

In Table 2.2 is shown a summary of the spatial configuration covered in these simulations. The range of the x parameter ($[0 : R]$) is subdivided into 20 steps, each with a size of 0.05 R, where R represents the tank radius. For each position, hits are simulated with θ ranging from 0° to 75° in increments of $\delta\theta = 5°$. The second angle, ϕ, is scanned over four possible values, 90°, 120°, 150°, or 180°, for a total of 1280 hit configurations.

	x (cm)	y (cm)	z (cm)	θ	$\delta\theta$	ϕ	$\delta\phi$	N points
p0	0	0	h	[0° : 75°]	5°	180°		16
p1	0.05R	0	h	[0° : 75°]	5°	[90° : 180°]	30°	64
p2	0.1R	0	h	[0° : 75°]	5°	[90° : 180°]	30°	64
p3	0.15R	0	h	[0° : 75°]	5°	[90° : 180°]	30°	64
p4	0.2R	0	h	[0° : 75°]	5°	[90° : 180°]	30°	64
p5	0.25R	0	h	[0° : 75°]	5°	[90° : 180°]	30°	64
p6	0.3R	0	h	[0° : 75°]	5°	[90° : 180°]	30°	64
p7	0.35R	0	h	[0° : 75°]	5°	[90° : 180°]	30°	64
p8	0.4R	0	h	[0° : 75°]	5°	[90° : 180°]	30°	64
p9	0.45R	0	h	[0° : 75°]	5°	[90° : 180°]	30°	64
p10	0.5R	0	h	[0° : 75°]	5°	[90° : 180°]	30°	64
p11	0.55R	0	h	[0° : 75°]	5°	[90° : 180°]	30°	64
p12	0.6R	0	h	[0° : 75°]	5°	[90° : 180°]	30°	64
p13	0.65R	0	h	[0° : 75°]	5°	[90° : 180°]	30°	64
p14	0.7R	0	h	[0° : 75°]	5°	[90° : 180°]	30°	64
p15	0.75R	0	h	[0° : 75°]	5°	[90° : 180°]	30°	64
p16	0.8R	0	h	[0° : 75°]	5°	[90° : 180°]	30°	64
p17	0.85R	0	h	[0° : 75°]	5°	[90° : 180°]	30°	64
p18	0.9R	0	h	[0° : 75°]	5°	[90° : 180°]	30°	64
p19	0.95R	0	h	[0° : 75°]	5°	[90° : 180°]	30°	64
p20	R	0	h	[0° : 75°]	5°	] 90° : 180°]	30°	48
total								1280

Table 2.2: Hit configurations simulated.

The particles examined in this study are primarily electrons and muons. Figure 2.4 shows the typical energy distributions for the electron and muon components of the shower particles interacting with the array tanks [Lui23]. These histograms illustrate the distributions for both γ-ray and proton showers. The considered energy of the primary particle ranges from 0.1 to 1 PeV, while the zenith angle (zd) denotes the incident angle at which the particle interacts with the atmosphere ($zd = 0$ represents a particle entering the atmosphere perpendicular to the ground). The position of the peaks remains consistent as the energy of the primary particle changes. For electrons, the energy distribution follows a bell-shaped curve with a tail extending to high energies, leading to an overlap in energy ranges with muons. The number of detected electrons is greater for γ-ray showers than for proton showers, but the peak energy remains approximately the same (around 0.04 GeV). In contrast, for muons there is a higher particle production in proton showers. When the primary particle is a proton, the energy peak also shifts slightly towards higher energies (around 1 or 10 GeV).[Lui23].
The vertical lines shown in Figure 2.4 denote the energy values considered for the simulated electrons and muons, covering the entire energy distribution. These selected values are also listed in Table 2.3.

Particle type	**Simulated energies [GeV]**
Electron	0.003 0.03 0.3 3
Muon	0.3 1 10 50 200

Table 2.3: Energy values considered for the simulations.

For both particles, an energy value around the peak and two more values corresponding to roughly the full width at half maximum, are chosen. The remaining energies are selected to sample the low and high-energy tails. However, for electrons, a fifth value below 0.003 GeV is not simulated because such a low-energy particle produces a very small signal in the tanks.

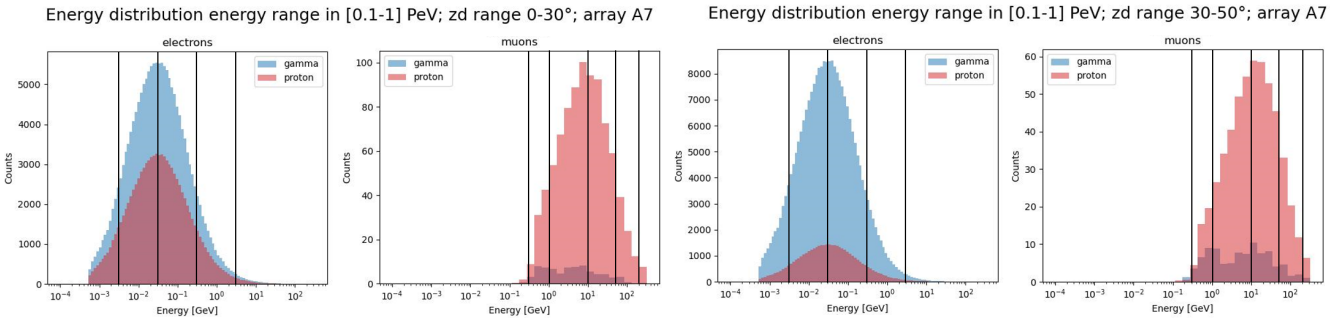

Figure 2.4: Energy distributions for electrons and muons [Lui23].

3. Data analysis and results

Among the output parameters provided by `HAWCSim` to describe the tank response, this thesis focuses on `HAWCSim.Evt.nPE`. It quantifies the total number of photo-electrons (PE) generated at the photo-cathode of the PMT per event (in our case, an event consists of a single *water-hit*, which indicates an individual particle reaching the tank water). The number of PE is directly related to the intensity of Cherenkov light generated in the single tank, later on used in combination with all other tanks to estimate the primary signal.

When a charged particle crosses a dielectric medium (with refractive index n) at a velocity greater than the speed of light in that medium (c/n), Cherenkov light is emitted. This emission occurs due to the in-phase reorientation of electric dipoles and results in a coherent wavefront at an angle θ, which defines the Cherenkov cone of light. The emission angle can be geometrically expressed as $\cos(\theta) = \frac{1}{\beta n_{water}}$, where $n_{water} = 1.33$ (the particle's velocity can be obtained from the relation $\beta = \sqrt{1-(\frac{mc^2}{E})^2}$ when the particle's energy E is known). The minimum velocity required for Cherenkov light emission is $\beta_{min} = 1/n$, which corresponds to an energy threshold of $E_{th} = \frac{mc^2}{\sqrt{1-1/n^2}}$. This threshold is approximately 0.0007 GeV for electrons and around 0.16 GeV for muons [DP18].

As described in chapter 2, this study is based on the repeated simulation of single-particle hits. The `HAWCSim` simulation is run 100 times for each set of input parameters, sampling different particle types (muons and electrons), energies (with values from Figure 2.4) and spatial hit configurations (covering all cases listed in Table 2.2). Consequently, this approach results in a statistical distribution of output parameters for every scenario.

In order to limit a priori hypothesis, to each single-particle hit configuration is assigned the mean output value of these distributions, along with its corresponding standard deviation. This approach assumes that, for every set of input parameters, the 100 simulated values follow a Gaussian distribution. However, as will be discussed later, this assumption is overly simplistic.

In the plots presented in the next sections, these average values are depicted. Each plot is related to a single particle type and energy. The horizontal axis represents the distance x, the vertical axis represents the zenithal angle of incidence θ, and it'is created at a fixed angle ϕ. The palette indicates the average value of the output parameter over the repeated simulations. Moreover, the percentage written over each bin describes the relative error on the value (calculated as $\sigma_r = \frac{std}{mean} \cdot 100$).

As previously described, tank design A is a dual-layer unit with one PMT for each volume. In this study the PE detected by the upper PMT (described in section 3.1) and those detected by the lower PMT (described in section 3.2) are distinguished. This differentiation is crucial for studying the muon-tagging capability of the dual-layer design.

In the following sections, the main features of the plots will be presented. However, for a comprehensive view, all plots for each particle, energy, and configuration are included in Appendix A and Appendix B.

3.1 Number of photo-electrons (nPE) - Upper layer

From an overall view, the patterns observed in the plots can be categorized into three different cases.

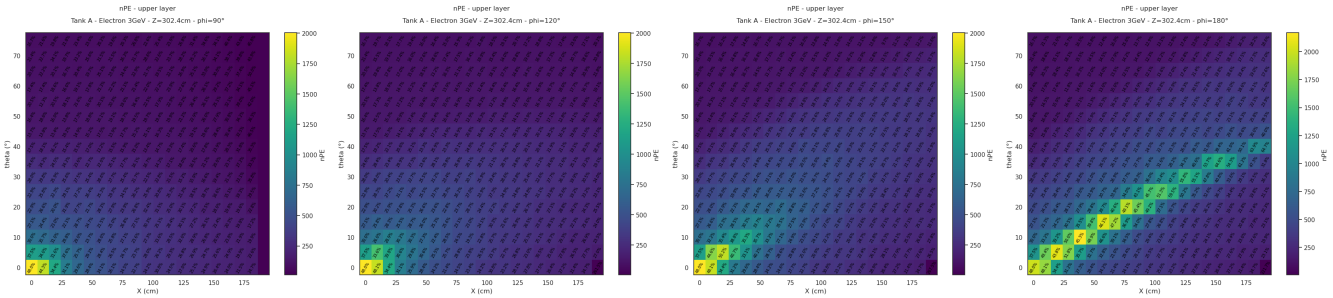

Figure 3.1: Number of photo-electrons detected in the upper layer for a 3 GeV electron (with fixed $\phi = 90°$, $\phi = 120°$, $\phi = 150°$ and $\phi = 180°$).

When the incident primary particle is energetic and high penetrating, it retains the majority of its energy travelling through the water. In such scenarios, the number of detected photo-electrons is significantly higher when the particle moves in the direction of the PMT (as illustrated in the diagonal stripe in Figure 3.1). These bins, characterized by intense signals, are arranged along a line within the $\phi_{180°}$ plane. The line starts at the configuration with $x = 0$ and $\theta = 0°$ (that represents a particle hitting the tank's center perpendicularly to its surface) and corresponds to larger θ values, as x increases, due to geometric factors.

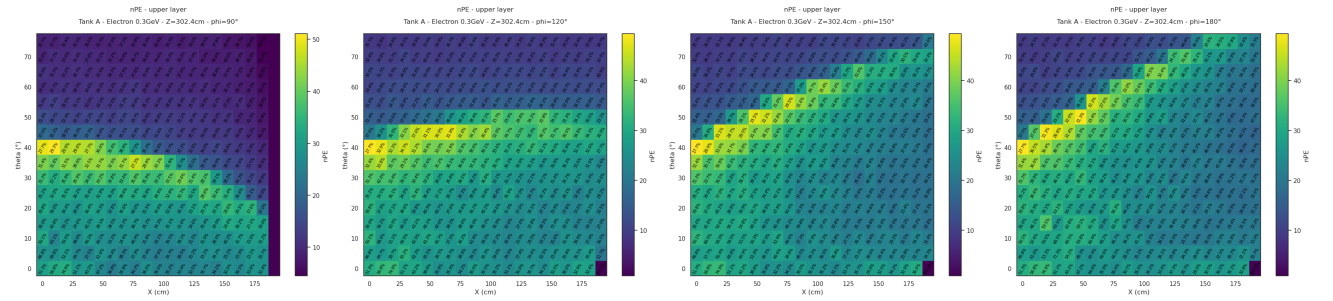

Figure 3.2: Number of photo-electrons detected in the upper layer for a 0.3 GeV electron (with fixed $\phi = 90°$, $\phi = 120°$, $\phi = 150°$ and $\phi = 180°$).

If the particle is less penetrating, it interacts with the water losing a significant portion of its energy. In such cases, the detected signal reveals the Cherenkov cone of light emitted (as illustrated in Figure 3.2). In this situation, the number of photo-electrons detected by the PMT follows the distribution of the Cherenkov photons. The bins aligned with the $\theta_{Cherenkov}$ angle exhibit an intense signal. If the particle has enough energy, the bins within the region covered by the Cherenkov cone also display an intense signal, as the particles continue emitting Cherenkov light while travelling through the water. However, an important differentiation should be made based on the parti-

cle type. If the particle hitting the tank is a muon, a single distinct Cherenkov cone is emitted. Scattering effects account for the slight extension of this intense signal beyond the cone section. On the other hand, if the particle is an electron, it also generates a particle shower, leading to a less distinct signal.

When the particle's energy is too low (around 1 MeV), the PMT detects almost no signal.

Table 3.1 provides a summary of the observed patterns based on particle type and energy, along with the expected Cherenkov angle and an indicator of the maximum value of the nPE output parameter detected in each case. The Cherenkov angle is estimated based on the first emission, occurring when the particle impacts the tank and hasn't lost any of its energy yet.

Particle Type	**Energy (GeV)**	β	$\theta_{Cherenkov}$	$nPE_{max}(average)$	**Pattern**	**Figure**
Electron	3	~ 0.999	$\sim 41°$	~ 2100	Direct Hit Line	I plot of Figure 3.4
	0.3	~ 0.999	$\sim 41°$	~ 50	Cherenkov Cone	II plot of Figure 3.4
	0.03	~ 0.999	$\sim 41°$	~ 3.5	Cherenkov Cone	III plot of Figure 3.4
	0.003	~ 0.985	$\sim 40°$	~ 0.16	Almost No Signal	IV plot of Figure 3.4
Muon	200	~ 0.999	$\sim 41°$	~ 1000	Direct Hit Line	I plot of Figure 3.3
	50	~ 0.999	$\sim 41°$	~ 900	Direct Hit Line	II plot of Figure 3.3
	10	~ 0.999	$\sim 41°$	~ 900	Direct Hit Line	III plot of Figure 3.3
	1	~ 0.994	$\sim 40°$	~ 700	Direct Hit Line	VI plot of Figure 3.3
	0.3	~ 0.936	$\sim 36°$	~ 25	Cherenkov Cone	V plot of Figure 3.3

Table 3.1: Summary of observed patterns, max nPE values and expected Cherenkov angles (based on particle type and energy).

Regarding muons, Figure 3.3 shows plots of the number of photo-electrons detected by the upper PMT at decreasing energies (200 GeV, 50 GeV, 10 GeV, 1 GeV, and 0.3 GeV). Muons, being highly penetrating particles, do not exhibit the Cherenkov cone pattern until their energy drops below 1 GeV, and they are consistently detected in the upper layer. At 0.3 GeV, the shape of the Cherenkov cone becomes visible, with an angle $\theta = 36°$, as estimated in Table 3.1.

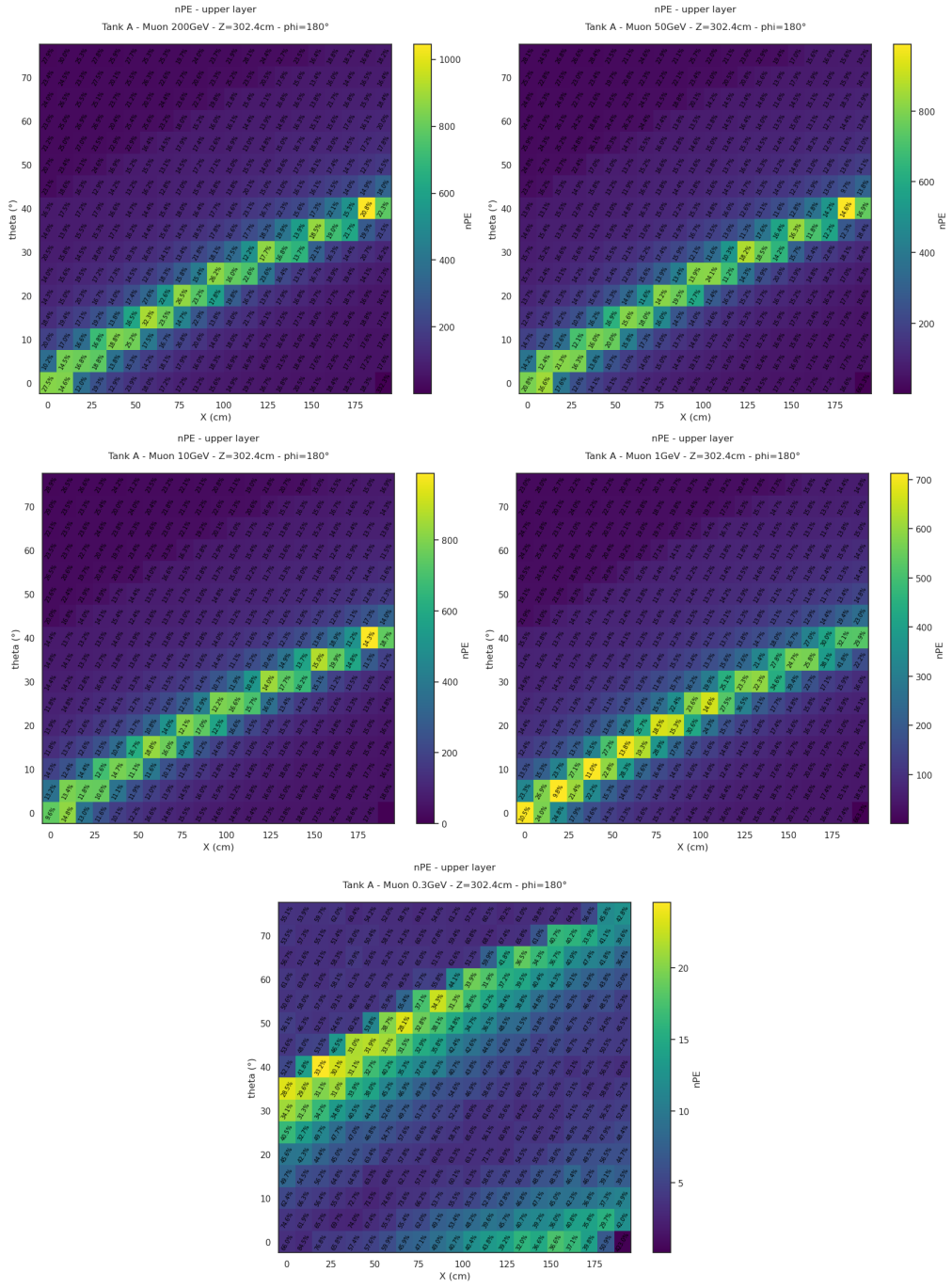

Figure 3.3: Number of photo-electrons detected in the upper layer for muons at decreasing energies (with fixed $\phi = 180°$).

The situation is different for electrons, as illustrated in Figure 3.4 with decreasing energies of 3 GeV, 0.3 GeV, 0.03 GeV, and 0.003 GeV. Only the most energetic among the simulated electrons display an intense signal aligned with the PMT direction. In the majority of cases, however, the number of detected photo-electrons follows the shape of the Cherenkov cone, with an angle $\theta = 41°$, as estimated in Table 3.1. In general, the detected signal is lower compared with muons, and electrons with an energy of 0.003 GeV or below do not produce a significant response in the tank unit.

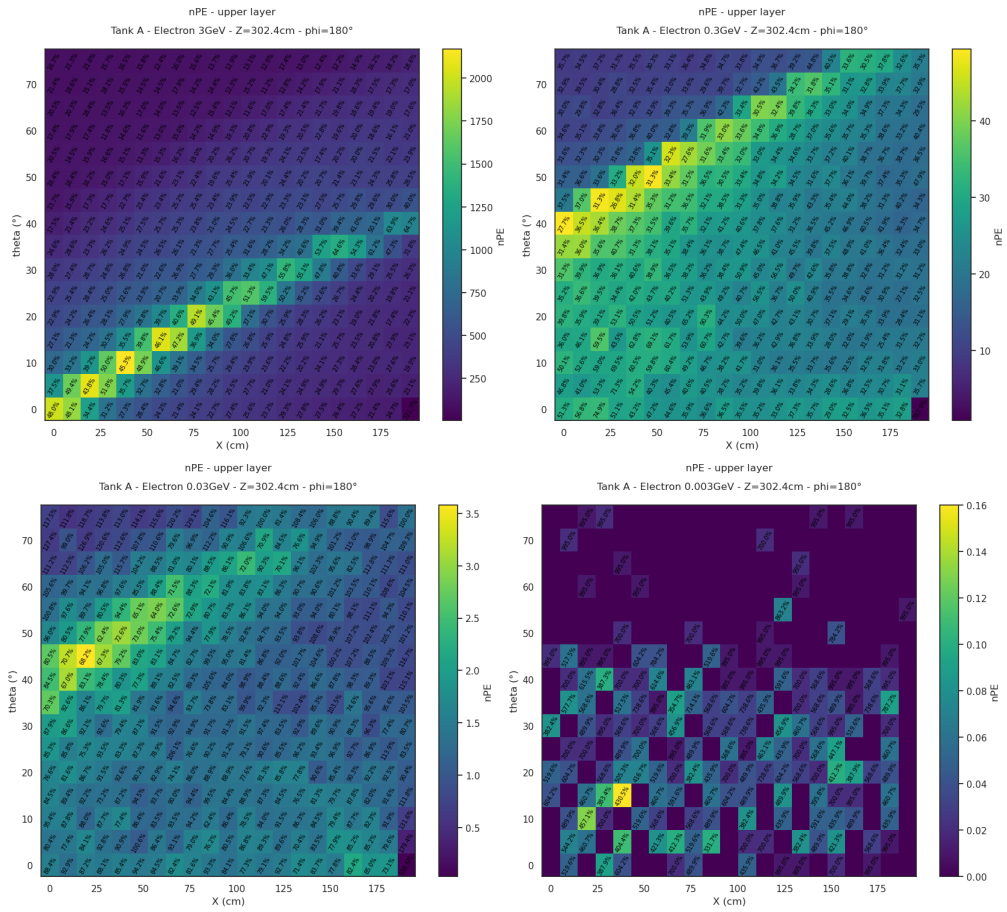

Figure 3.4: Number of photo-electrons detected in the upper layer for electrons at decreasing energies (with fixed $\phi = 180°$).

Looking at the nPE_{max} values in Table 3.1, it's clear that the intensity of the detected signal increases with the energy of the particle. Muons are simulated with much higher energies than electrons, resulting in higher typical nPE values for them. However, when comparing the two particle types at similar energies, it appears that the response for electrons is slightly greater. This difference may be attributed to the fact that, as mentioned earlier, a muon interacting with water leads to the emission of a single Cherenkov cone, whereas an electron impact is associated with the production of an additional particle shower, the components of which can also emit Cherenkov light.
It's important to point out that the parameter values shown in these plots represent the averages of distributions derived from repeated simulations, assuming a Gaussian distribution.

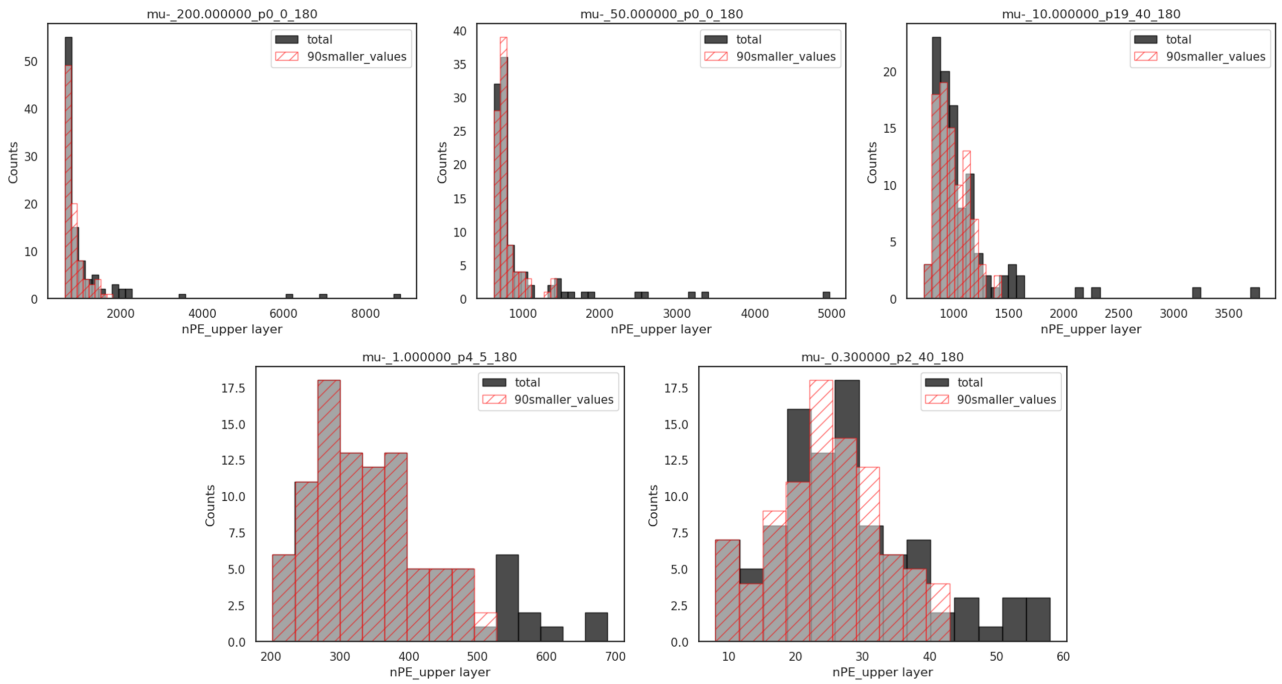

Figure 3.5: Histograms of nPE distributions for some muon configurations with decreasing energies (upper layer).

However, looking at the histograms of these values for some of the simulated configuration (represented in Figure 3.6 for electrons and in Figure 3.5 for muons), it becomes evident that this assumption may not be statistically accurate. This observation is further supported by the substantial relative errors associated with each bin, which are sometimes extremely high, exceeding 100%. In many cases, the Gaussian nature of the distributions appears to be compromised by a tail of exceptionally high nPE values. These unusually high values seem to occur primarily in scenarios involving a direct hit. They could be associated with the simulation's response to a particle physically passing through the PMT.

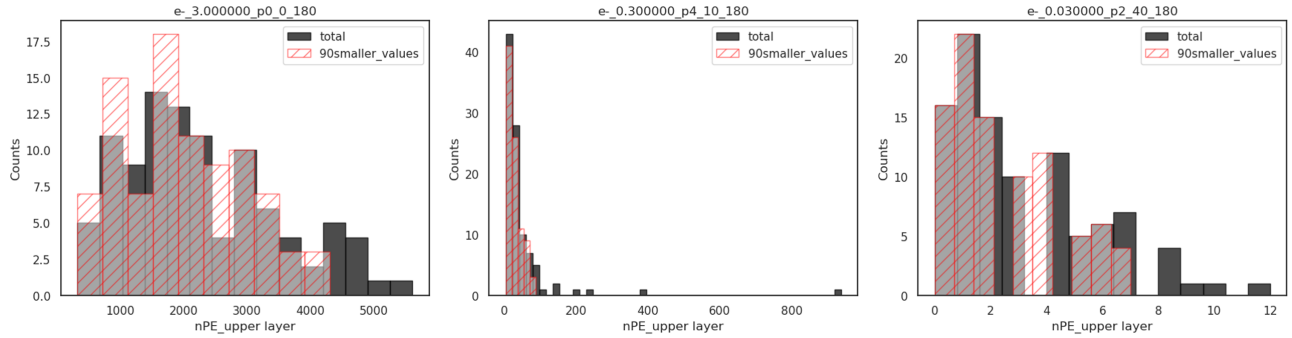

Figure 3.6: Histograms of nPE distributions for some electron configurations with decreasing energies (upper layer).

To address this issue, an initial approach is to calculate the average by considering only the 90 smallest values

from each set of simulations. This is done to exclude the data in the tail and to obtain an average value that better represents the detector's response in the majority of cases. The output values displayed in the previously discussed plots are obtained using this method, excluding the 10 largest values from the computation.
Considering the values in Table 3.1 related to the most energetic particles, it's also evident that the signal produced by a 3 GeV electron (with $nPE_{max} \sim 2100$) is larger than the one associated with a 200 GeV muon (with $nPE_{max} \sim 1000$). This outcome could once again be linked to the variations in how these particles interact with water (and with the production of a shower of secondary particles in the first case). When examining the histograms in Figure 3.6 and Figure 3.5, it becomes clear that this distinction could also be associated with the decision to exclude the top 10 values from the average. Specifically, the distribution for 3 GeV electrons consists primarily of values exceeding nPE = 1000. Consequently, the reduction of the analyzed sample size has a limited impact on the average value. In contrast, for 200 GeV muons the tail of high nPE values is more pronounced. In this case, due to the applied simplification, information related to exceptionally high values (exceeding those observed for electrons, i.e., over 2000) is lost.

3.2 Number of photo-electrons (nPE) - Lower layer

In the case of the lower layer, the scenario is much simpler. Only particles with sufficient energy to pass through the upper layer and reach the lower volume are detected by the PMT. This condition excludes particles that dissipate all their energy before, emitting the Cherenkov light cone detected by the upper PMT.
If the primary particle hitting the tank reaches the lower layer, the number of detected photo-electrons is significantly higher when the particle moves in the direction of the PMT. These bins, characterized by intense signal, are again arranged along a line within the ϕ_{180° plane (as depicted in Figure 3.9 and Figure 3.10). Due to the different position of this second PMT, as illustrated in Figure 2.2 and Figure 2.1, this direct-hit line corresponds to lower θ values than before, and doesn't intersect the $x = 0$-$\theta = 0^\circ$ configuration.

Particle Type	**Energy (GeV)**	nPE_{max} **(average)**	**Figure**
Electron	3	~ 300	I plot of Figure 3.8
	0.3	~ 6	II plot of Figure 3.8
	0.03	No significant signal	III plot of Figure 3.8
	0.003	No significant signal	
Muon	200	~ 500	I plot of Figure 3.7
	50	~ 400	II plot of Figure 3.7
	10	~ 350	III plot of Figure 3.7
	1	~ 160	VI plot of Figure 3.7
	0.3	No significant signal	V plot of Figure 3.7

Table 3.2: Summary of max nPE values for the lower layer (based on particle type and energy).

Figure 3.7 shows plots of the number of photo-electrons detected by the upper PMT for muons at decreasing energies (200 GeV, 50 GeV, 10 GeV, 1 GeV, and 0.3 GeV). Once again, being highly penetrating particles, they generate a strong signal along the PMT direction in nearly all cases. They are not detected only for energies around 0.3 GeV and below, which corresponds to the scenario where a Cherenkov cone was exhibited in the upper layer. As also summarized in Table 3.2, the signal intensity increases with the particle's energy.

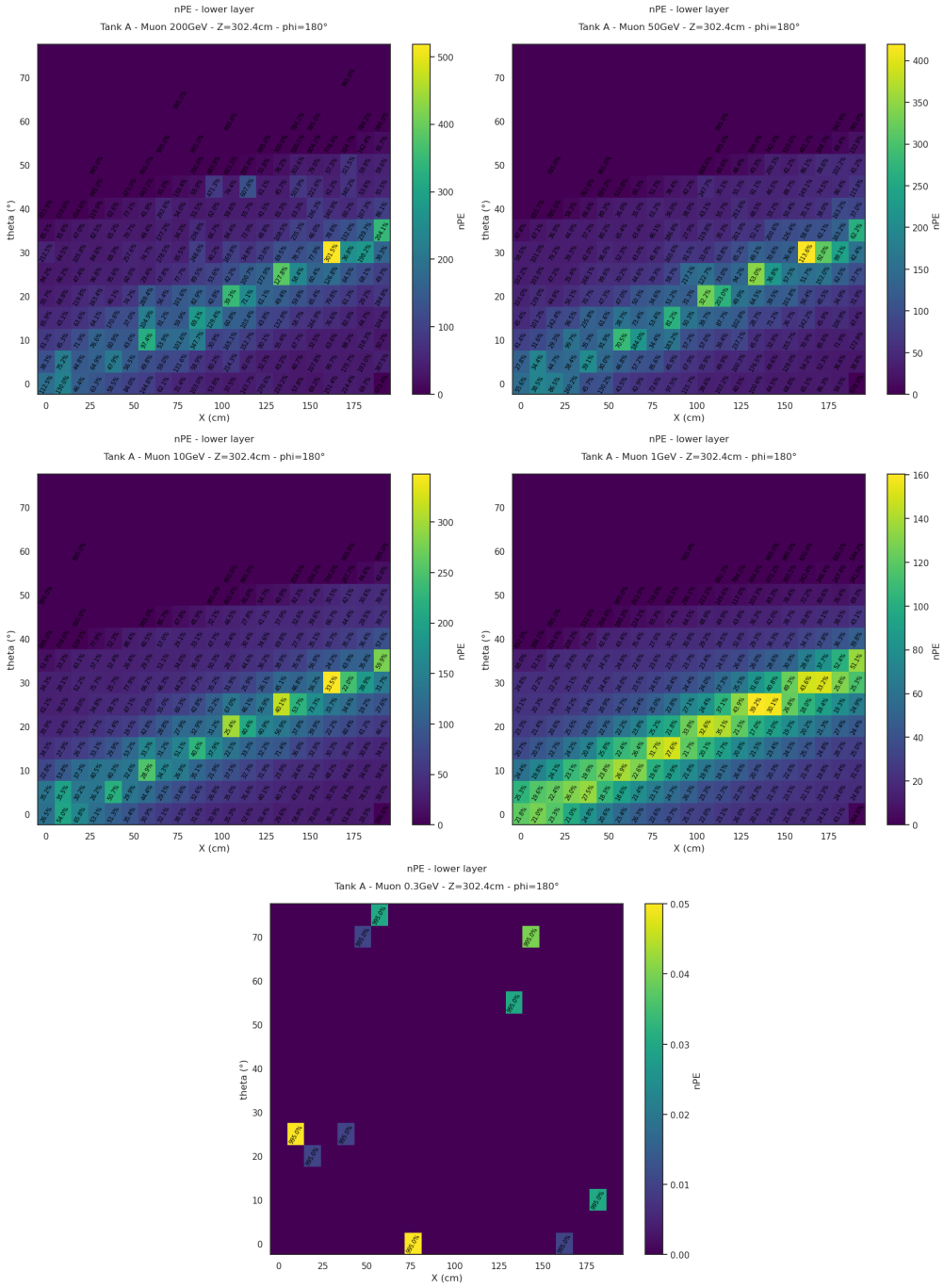

Figure 3.7: Number of photo-electrons detected in the lower layer for muons at decreasing energies (with fixed $\phi = 180°$).

The expected muon-tagging capability of the dual-layer design is based on the assumption that electrons are not enough penetrating to leave a signal in the lower volume. If this were indeed the case, a signal detected by the lower PMT would be attributed to the passage of a muon. However, as depicted in the plots of Figure 3.8, this discrimination process is observed to be effective only for electrons below a specific energy threshold.

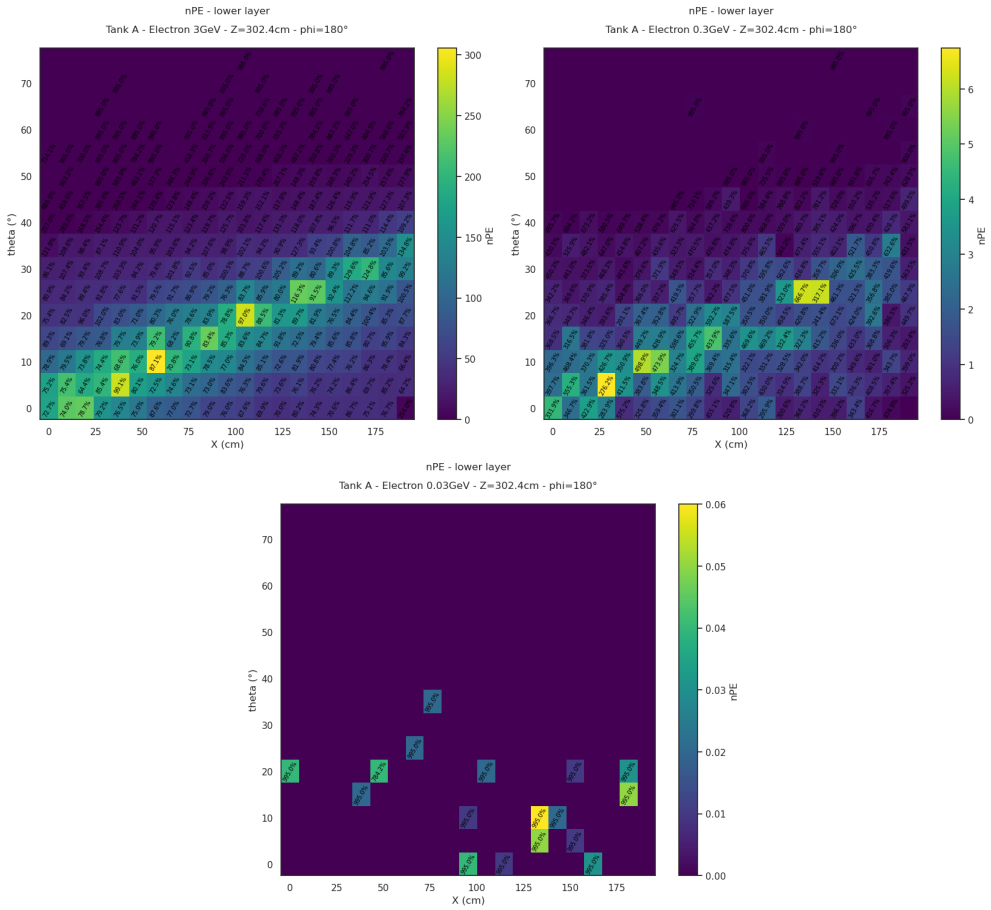

Figure 3.8: Number of photo-electrons detected in the lower layer for electrons at decreasing energies (with fixed $\phi = 180°$).

When a 3 GeV electron hits the tank, a strong signal is detected by the lower PMT. This is a predictable outcome as, at these energy levels, the nPE plots in the upper layer do not display the characteristic Cherenkov cone shape (0.3 GeV electrons also appear to reach the lower layer, although the signal they generate is not significant when compared to other particles). The detection of electrons in the lower layer has the potential to affect the detector's capability to differentiate between electromagnetic and hadronic showers. As illustrated in Figure 2.4, although the detection of electrons at these energies is relatively limited, it remains a possibility.
A closer examination of the signals produced by a 3 GeV electron and a 1 GeV muon reveals striking similarities in the detector's response, both in the lower and upper layers. Figure 3.9 and Figure 3.10 present comprehensive plots of the nPE parameter for the lower layer at all fixed values of ϕ.

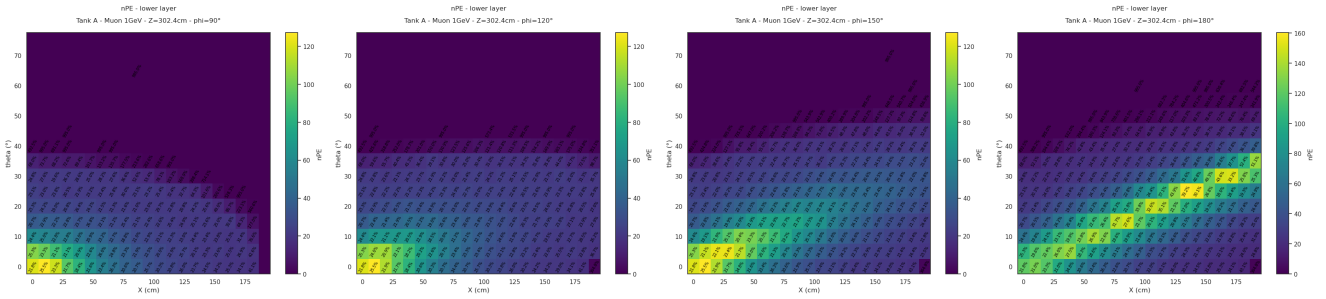

Figure 3.9: Number of photo-electrons detected in the lower layer for a 1 GeV muon (with fixed $\phi = 90°$, $\phi = 120°$, $\phi = 150°$ and $\phi = 180°$).

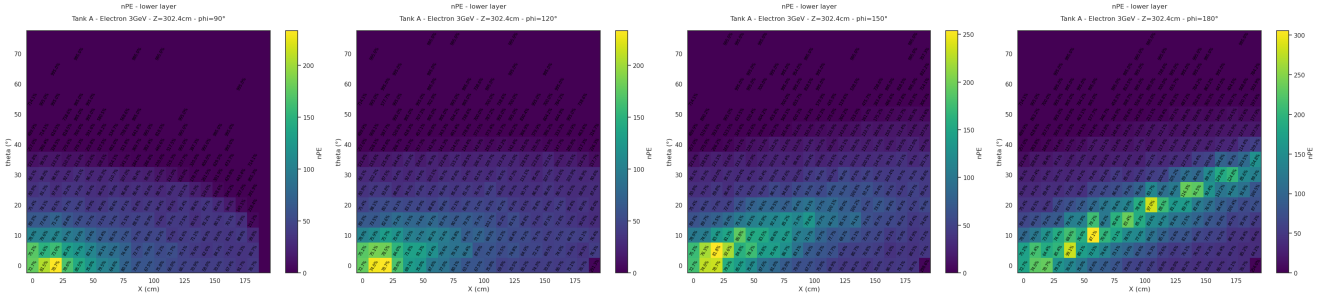

Figure 3.10: Number of photo-electrons detected in the lower layer for a 3 GeV electron (with fixed $\phi = 90°$, $\phi = 120°$, $\phi = 150°$ and $\phi = 180°$).

This tail in the electron energy distribution, which extends to high energies and results in an overlap in energy ranges with muons, must be carefully considered to understand the detector's response.

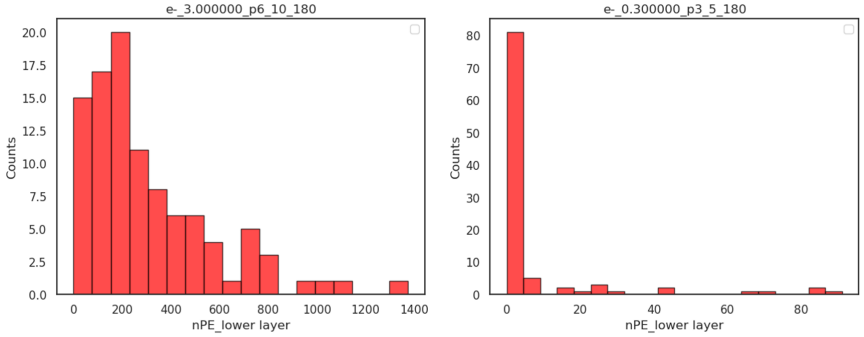

Figure 3.11: Histograms of nPE distributions for some electron configurations with decreasing energies (lower layer).

From a general overview of the nPE histograms for some of the simulated configurations (represented in Figure 3.11 for electrons and in Figure 3.12 for muons), it becomes also evident that the assumption of a Gaussian distribution is even less realistic for the lower layer.

In the plots presented in this section, all output values are included in the calculation of the average.

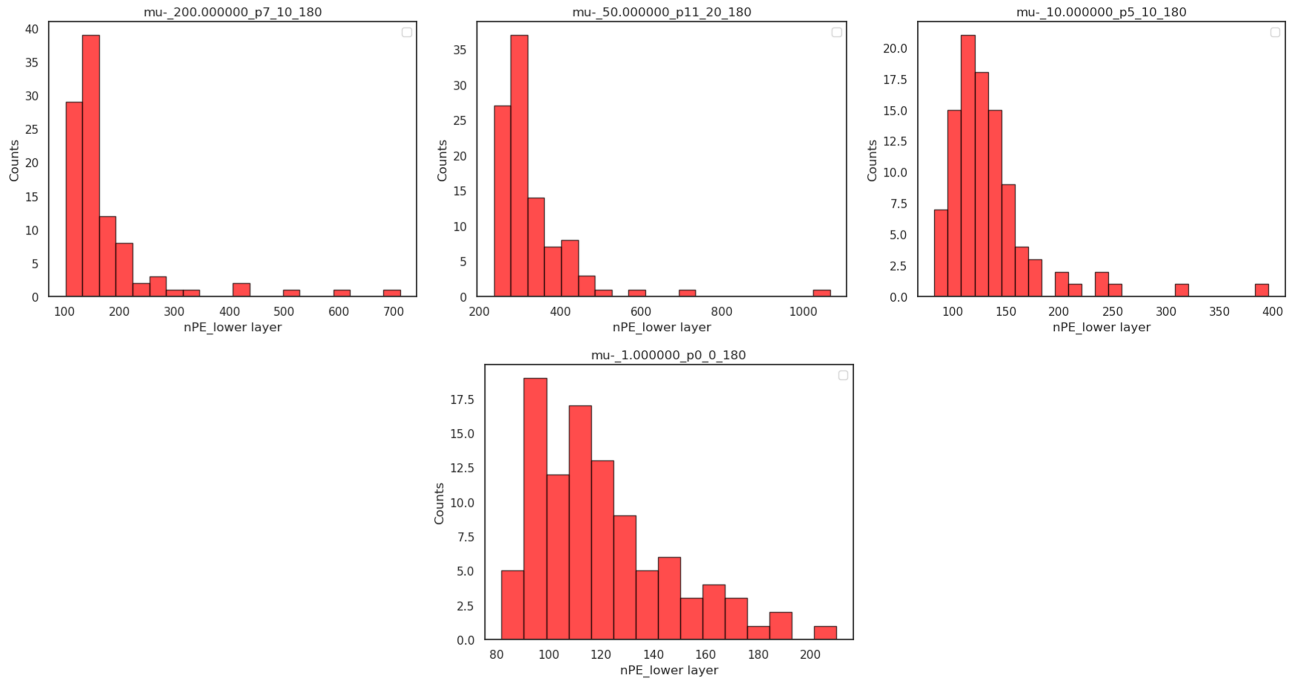

Figure 3.12: Histograms of nPE distributions for some muon configurations with decreasing energies (lower layer).

4. Conclusions

This study demonstrates that the tank's response to a single-particle hit, analyzed through the number of generated photo-electrons, is significantly influenced by the particle's energy and the specific geometric configuration of the water-hit. A difference in the energy and type of the particle, results in variations both in the output values for each bin and in the overall pattern observed in the plot. As a consequence, in most cases there is a discernible difference in the response between an electron hit and a muon hit. This differentiation primarily arises from the fact that the energy distributions of these particles, when they reach the detector array, exhibit only slight overlaps.

As mentioned before, in order to study the muon-tagging capability of the dual-layer design, a separate analysis of PE detected by the upper and the lower PMT is carried out. This discrimination process is based on the assumption that electrons are not enough penetrating to leave a signal in the lower volume. However, according to the data, this assumption shows to be realistic only for electrons below a specific energy threshold. The limitations of this approach become evident dealing with electrons that populate in the high-energy tail of the distribution, particularly when their energies are comparable to those of muons. In fact, a closer examination of the signals produced by a 3 GeV electron and a 1 GeV muon reveals striking similarities, both in the lower and upper layers. The detection of electrons in the lower layer has the potential to affect SWGO capability to differentiate between electromagnetic and hadronic showers. On the other hand, these energy values for electrons are statistically much less frequent.

Another consideration needs to be made regarding the assumption of a Gaussian distribution for the output values, which appears to be statistically inaccurate in most cases. Theoretically, it would be possible to base the analysis on specific asymmetrical probability distributions (e.g., negative binomial distribution) accurately chosen to better fit the histogram distributions. In such a scenario, the Look-Up Tables could store information about these distributions for each bin, and for the output parameters, randomly sample values from the fitted distributions, rather than providing the average values. However, these choices would be somewhat arbitrary and not based on actual physical properties of the system. Adopting such distributions would entail extra a priori assumptions and could potentially introduce bias into the measurements. Therefore, this approach is not followed in this study.

This thesis is part of a larger project focused on the development of a more efficient parameterized simulation of the detector response, through the creation of Look-Up Tables. The ultimate goal is to analyze the response of SWGO to PeV atmospheric showers. This understanding is crucial during the observatory design phase to ensure that the future Southern Wide-field Gamma-ray Observatory achieves high sensitivity across a wide energy range, extending beyond a 100 TeV high-energy threshold.

After the recent promising detection of 12 UHE γ-ray Galactic sources by the LHAASO observatory, new instruments like SWGO, offering improved spatial, temporal, and spectral resolution in the PeV range, could potentially lead to a breakthrough in PeVatron identification and the search for the origin of cosmic rays. Thanks to these new observatories, it may finally be possible to identify those sources that constitute the most powerful astrophysical particle accelerators within our Galaxy.

Bibliography

[Alm21] Ulisses Barres de Almeida and. "*The Southern Wide-Field Gamma-ray Observatory*". In: *Astronomische Nachrichten* 342.1-2 (Jan. 2021), pp. 431–437. DOI: 10.1002/asna.202113946. URL: https://doi.org/10.1002%2Fasna.202113946.

[CG23] Martina Cardillo and Andrea Giuliani. "*The LHAASO PeVatron Bright Sky: What We Learned*". In: *Applied Sciences* 13.11 (May 2023), p. 6433. DOI: 10.3390/app13116433. URL: https://doi.org/10.3390%2Fapp13116433.

[Cri21] Pierre Cristofari. "*The Hunt for Pevatrons: The Case of Supernova Remnants*". In: *Universe* 7.9 (2021). ISSN: 2218-1997. DOI: 10.3390/universe7090324. URL: https://www.mdpi.com/2218-1997/7/9/324.

[DP18] Alessandro De Angelis and Mário Pimenta. *"Introduction to Particle and Astroparticle Physics"*. Multimessenger Astronomy and its Particle Physics Foundations. London: Springer, 2018.

[Dor09] Michele Doro. "*Novel Reflective Elements and Indirect Dark Matter Searches for MAGIC II and Future IACTs*". PhD thesis. Università degli studi di Padova, 2009. URL: http://hdl.handle.net/11577/3425635.

[Kac08] M. Kachelriess. *"Lecture notes on high energy cosmic rays"*. 2008. arXiv: 0801.4376 [astro-ph].

[LL92] M.S. Longair and M.S. Longair. *"High Energy Astrophysics: Volume 1, Particles, Photons and Their Detection"*. High Energy Astrophysics. Cambridge University Press, 1992. ISBN: 9780521387736. URL: https://books.google.it/books?id=GgFjLiZDOk8C.

[Lui23] Riccardo Lui. "*The PeV response of different proposed arrays of SWGO*". B.S. Thesis. University of Padua, 2023. URL: https://hdl.handle.net/20.500.12608/48895.

[RG41] Bruno Rossi and Kenneth Greisen. "*Cosmic-Ray Theory*". In: *Reviews of Modern Physics* 13.4 (Oct. 1941), pp. 240–309. DOI: 10.1103/RevModPhys.13.240.

[SWG22] SWGO. *"The Southern Wide-field Gamma-ray Observatory (SWGO)"*. https://www.swgo.org/SWGOWiki/doku.php?id=start. 2019 (accessed August 15, 2022).

Appendices

A nPE - upper layer

A.1 Electrons - 3 GeV

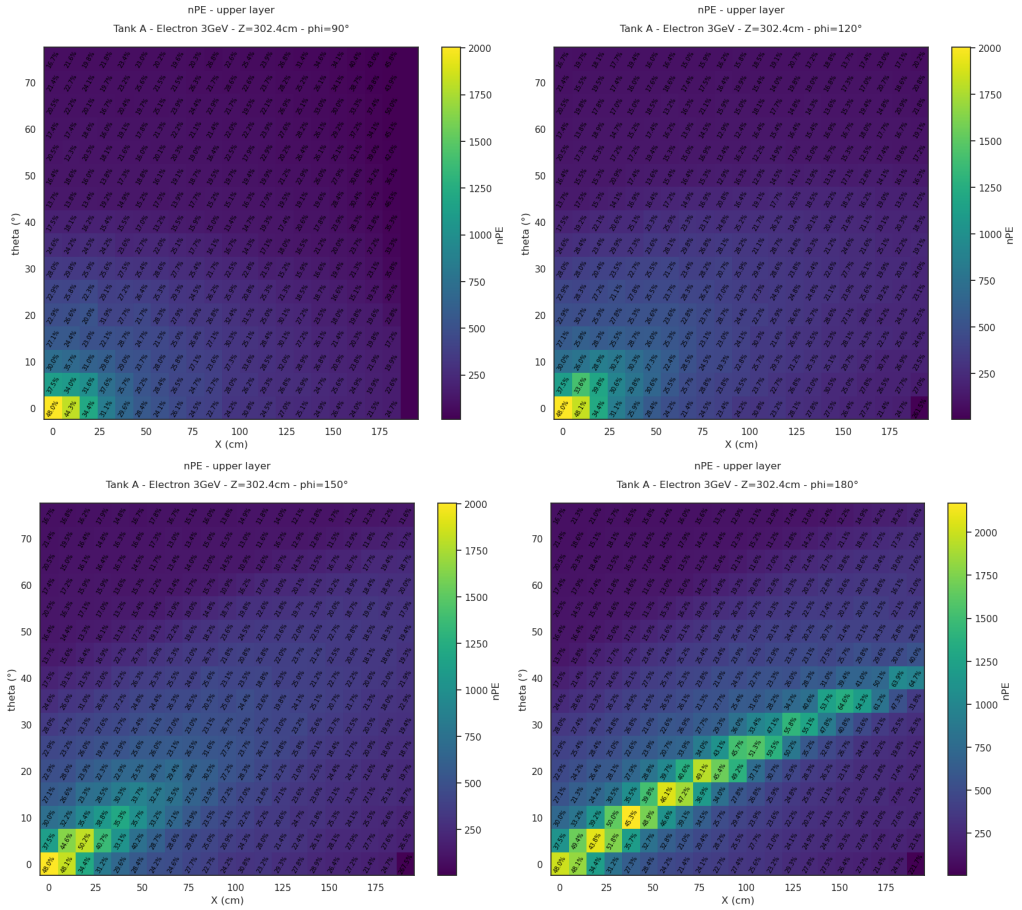

Figure 1: Number of photo-electrons detected in the upper layer for a 3 GeV electron (with fixed $\phi = 90°$, $\phi = 120°$, $\phi = 150°$ and $\phi = 180°$).

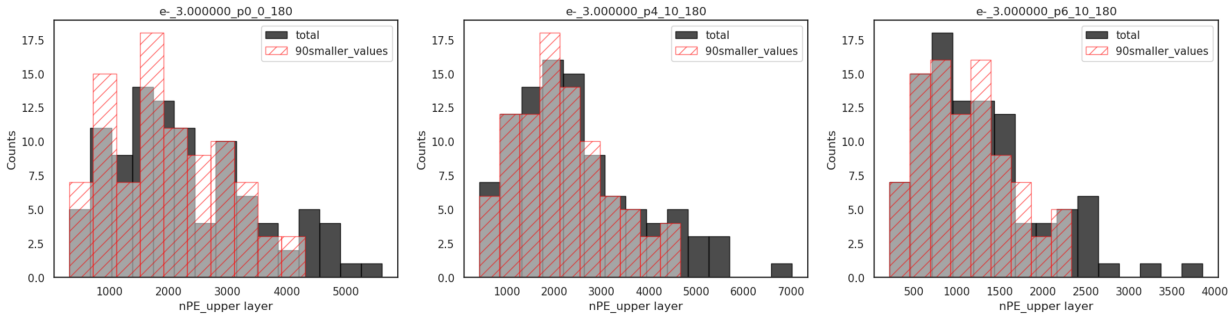

Figure 2: Histograms of nPE distributions for some 3 GeV electron configurations (upper layer).

A.2 Electrons - 0.3 GeV

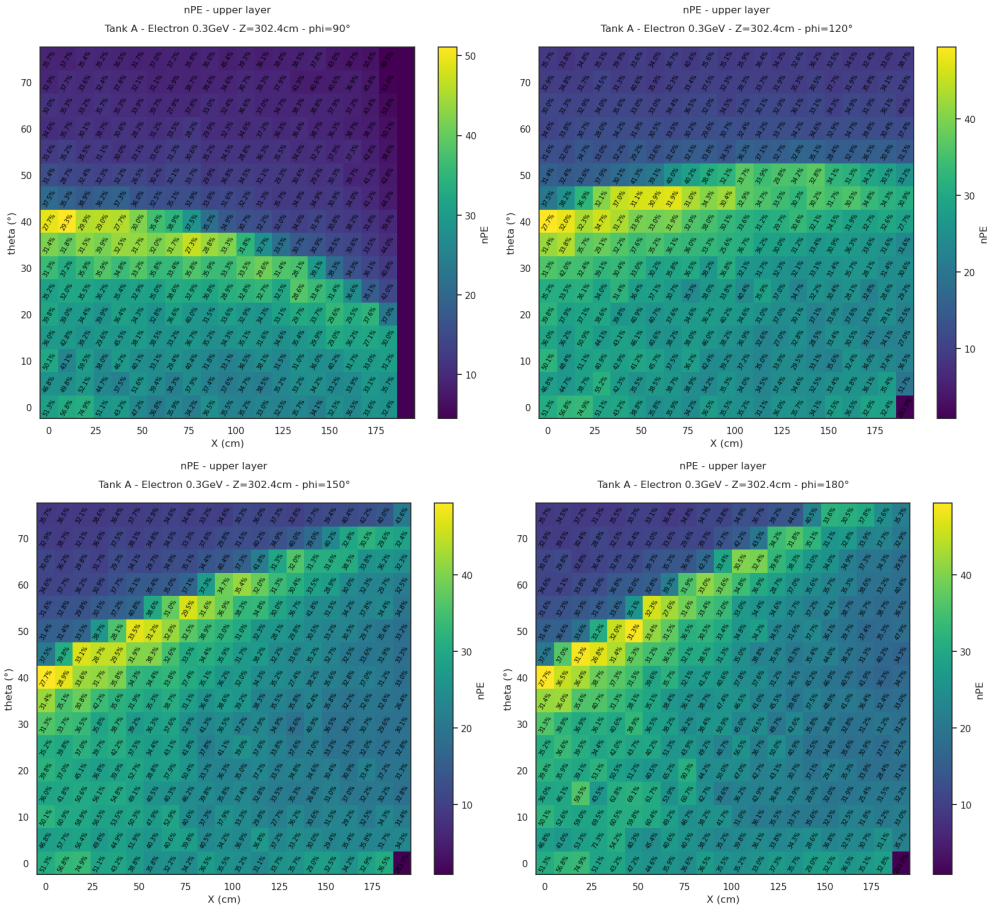

Figure 3: Number of photo-electrons detected in the upper layer for a 0.3 GeV electron (with fixed $\phi = 90°$, $\phi = 120°$, $\phi = 150°$ and $\phi = 180°$).

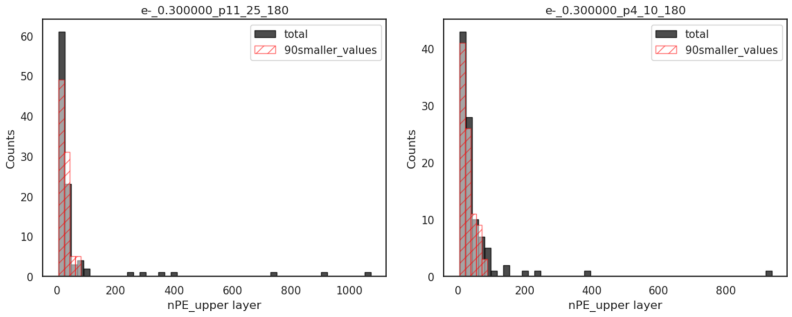

Figure 4: Histograms of nPE distributions for some 0.3 GeV electron configurations (upper layer).

A.3 Electrons - 0.03 GeV

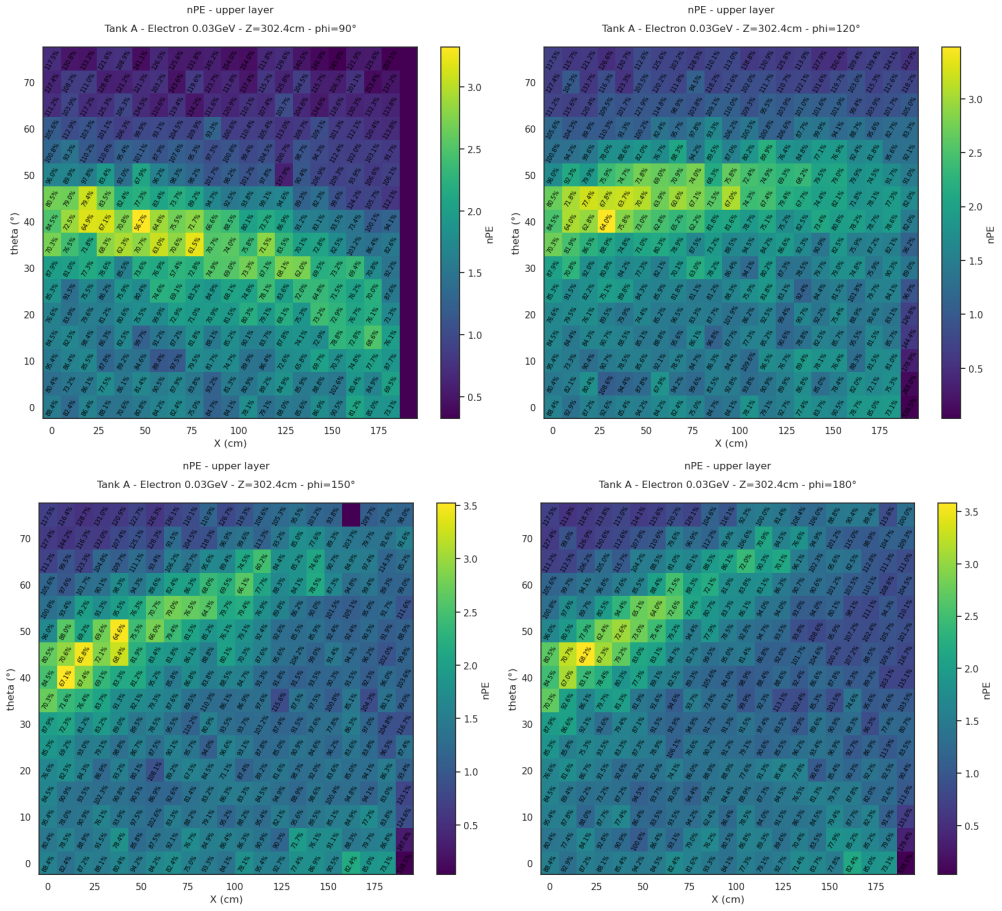

Figure 5: Number of photo-electrons detected in the upper layer for a 0.03 GeV electron (with fixed $\phi = 90°$, $\phi = 120°$, $\phi = 150°$ and $\phi = 180°$).

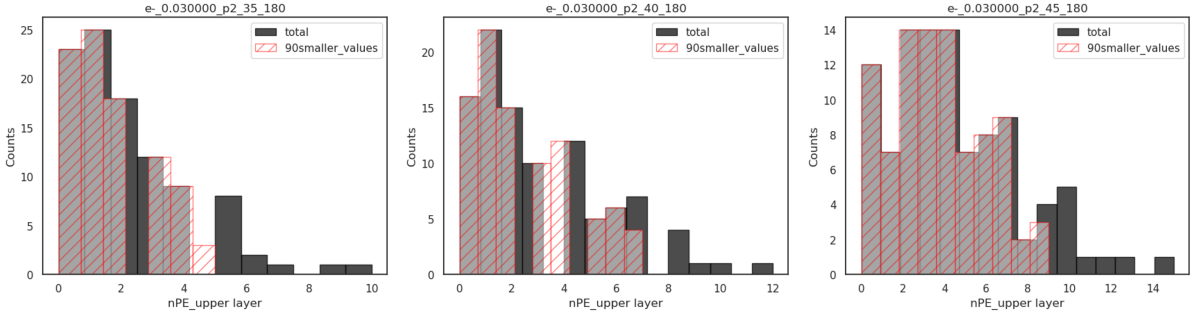

Figure 6: Histograms of nPE distributions for some 0.03 GeV electron configurations (upper layer).

A.4 Electrons - 0.003 GeV

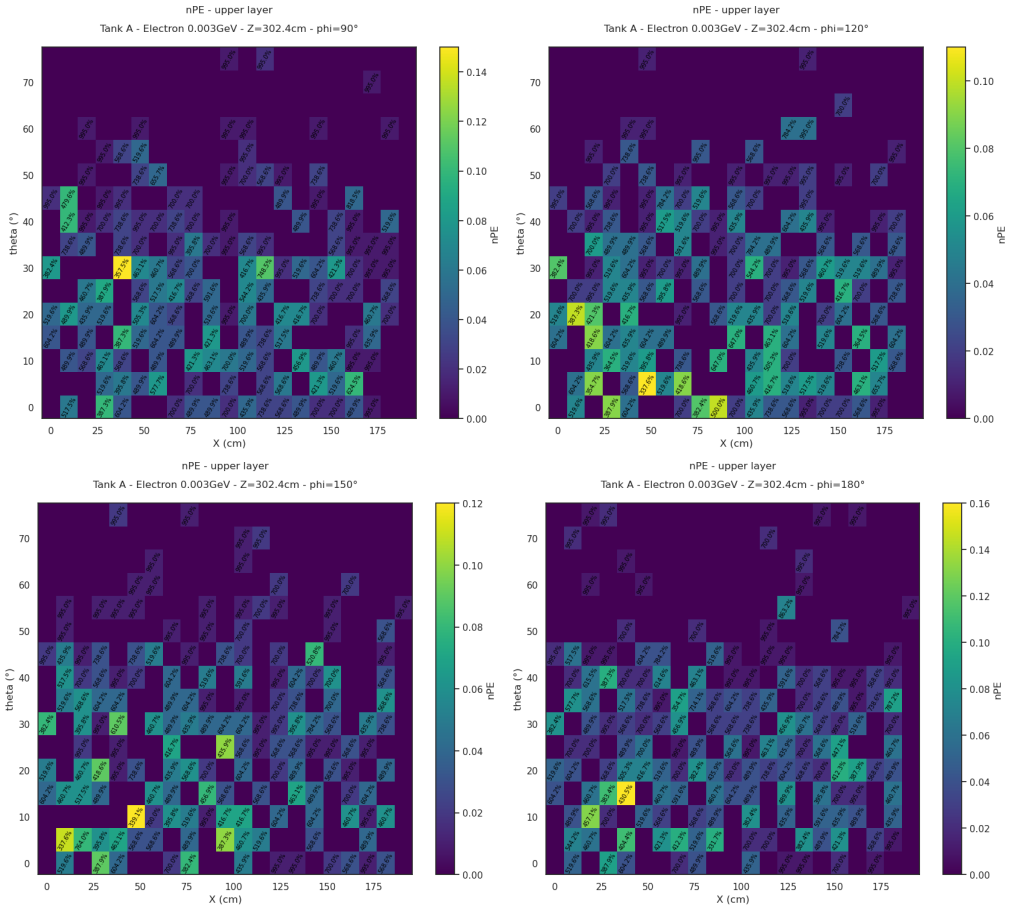

Figure 7: Number of photo-electrons detected in the upper layer for a 0.003 GeV electron (with fixed $\phi = 90°$, $\phi = 120°$, $\phi = 150°$ and $\phi = 180°$).

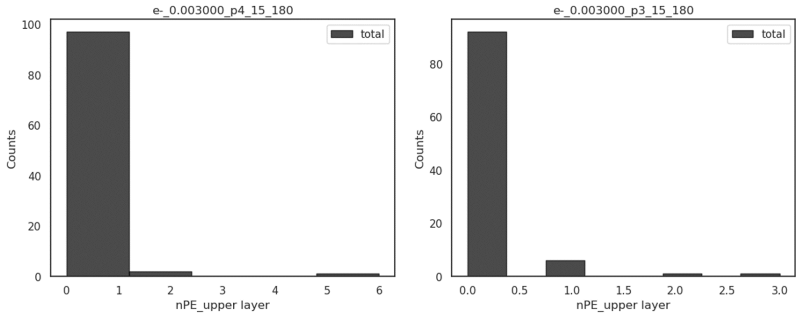

Figure 8: Histograms of nPE distributions for some 0.003 GeV electron configurations (upper layer).

A.5 Muons - 200 GeV

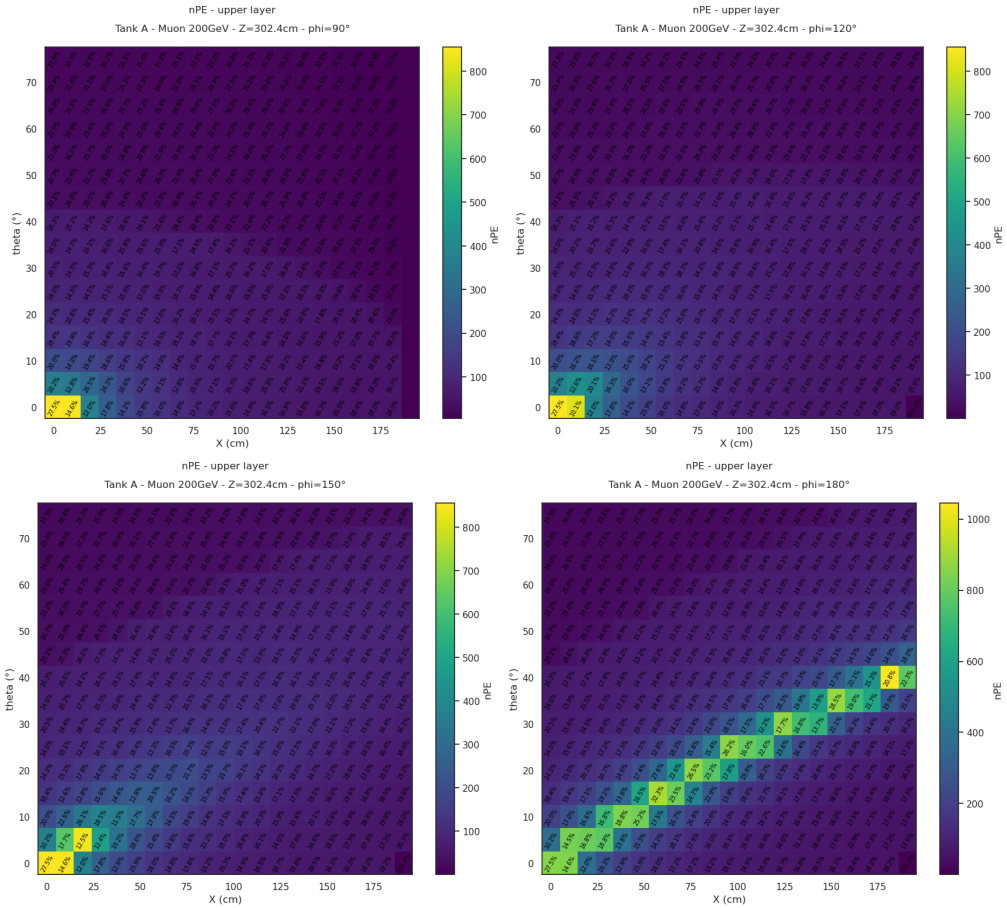

Figure 9: Number of photo-electrons detected in the upper layer for a 200 GeV muon (with fixed $\phi = 90°$, $\phi = 120°$, $\phi = 150°$ and $\phi = 180°$).

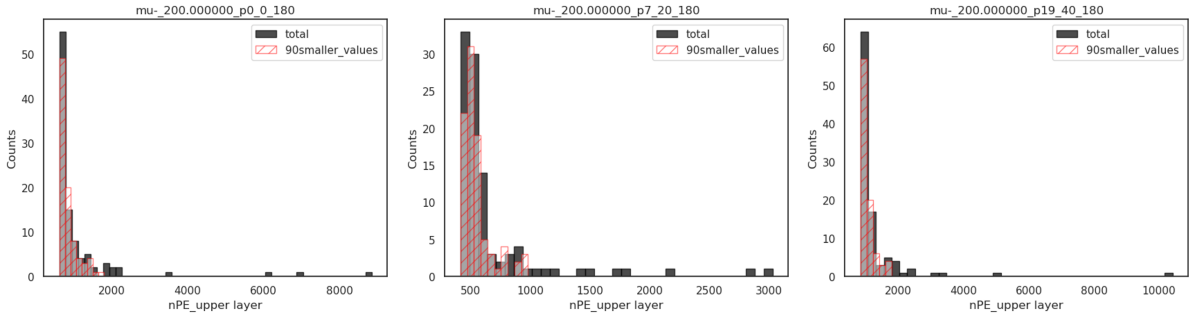

Figure 10: Histograms of nPE distributions for some 200 GeV muon configurations (upper layer).

A.6 Muons - 50 GeV

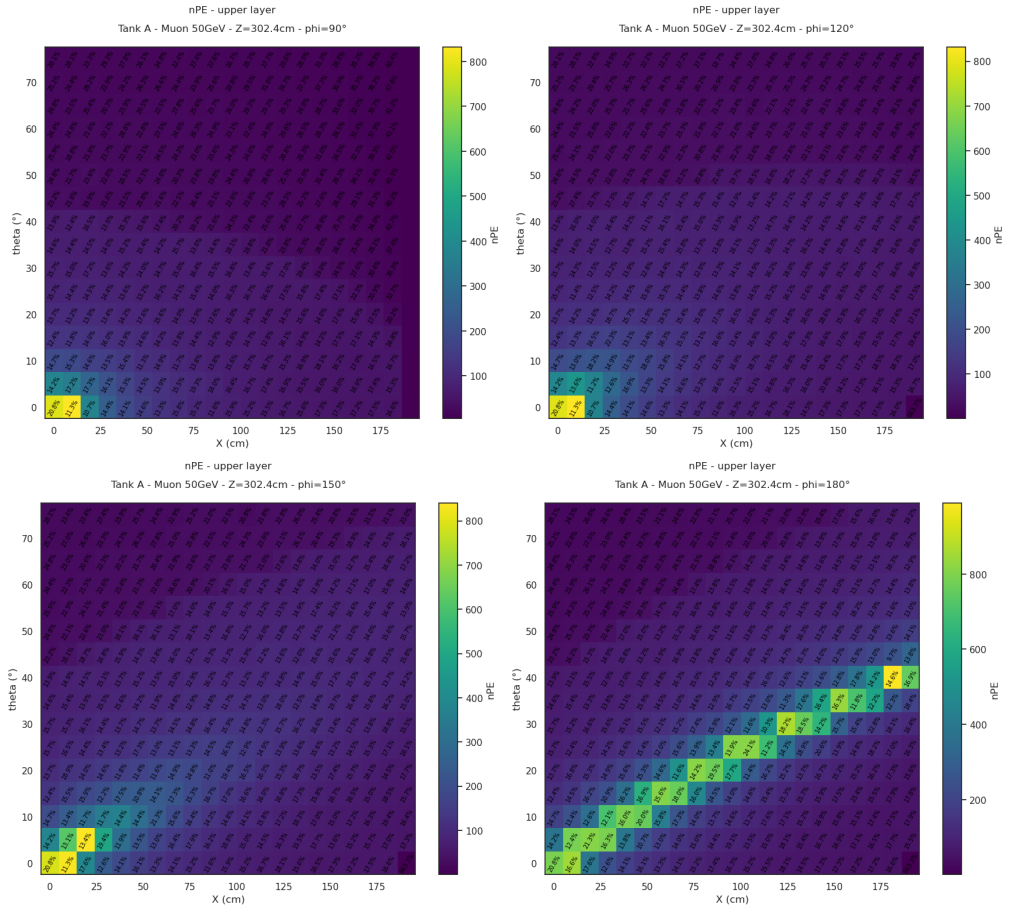

Figure 11: Number of photo-electrons detected in the upper layer for a 50 GeV muon (with fixed $\phi = 90°$, $\phi = 120°$, $\phi = 150°$ and $\phi = 180°$).

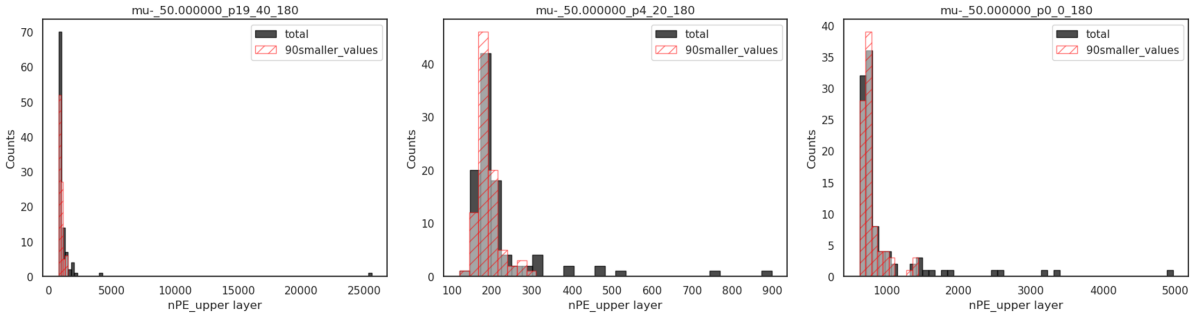

Figure 12: Histograms of nPE distributions for some 50 GeV muon configurations (upper layer).

A.7 Muons - 10 GeV

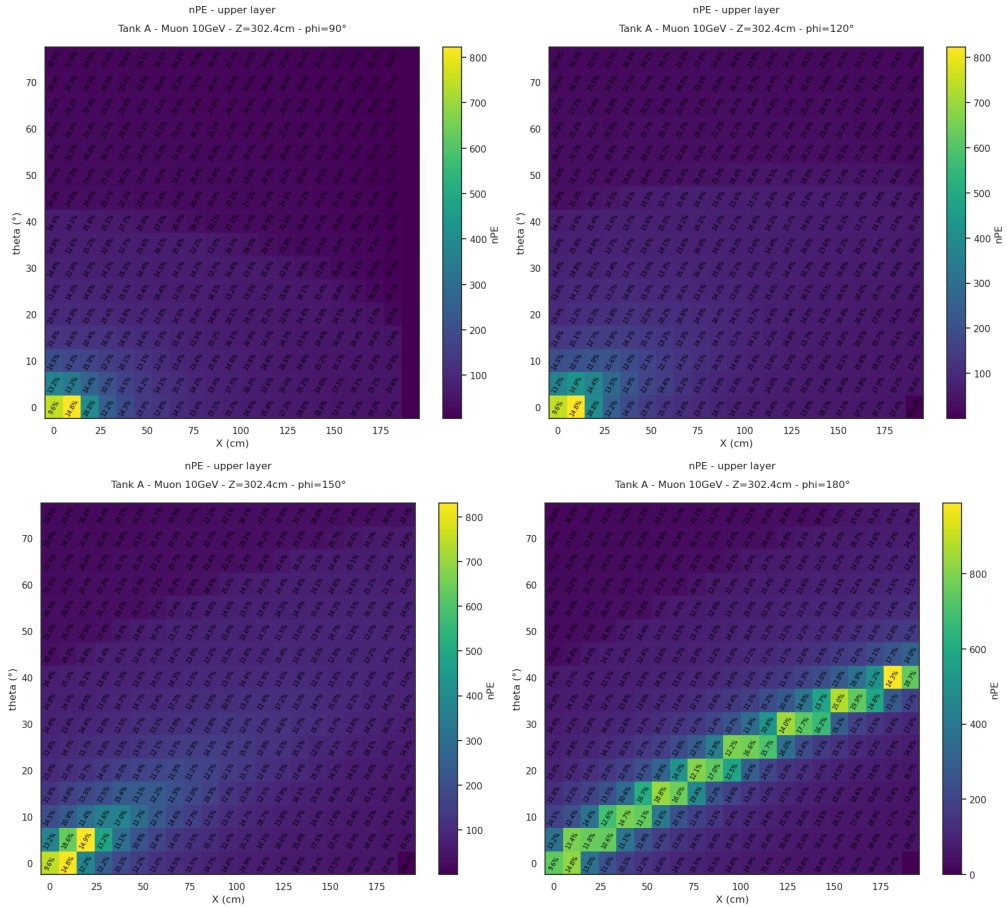

Figure 13: Number of photo-electrons detected in the upper layer for a 10 GeV muon (with fixed $\phi = 90°$, $\phi = 120°$, $\phi = 150°$ and $\phi = 180°$).

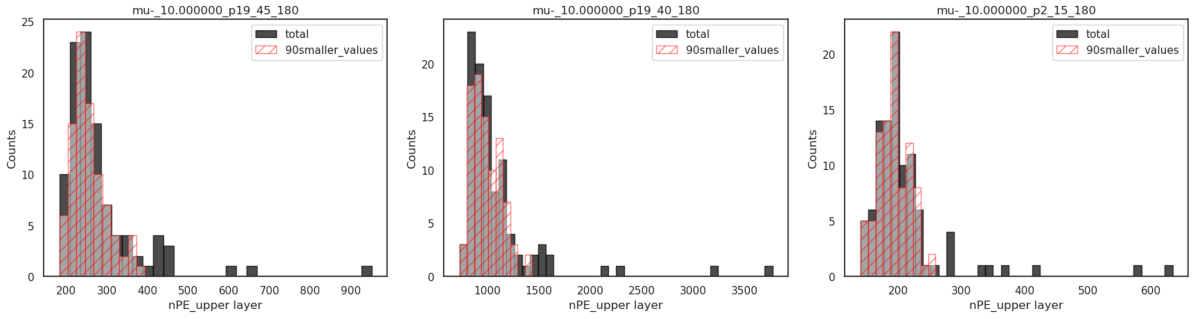

Figure 14: Histograms of nPE distributions for some 10 GeV muon configurations (upper layer).

A.8 Muons - 1 GeV

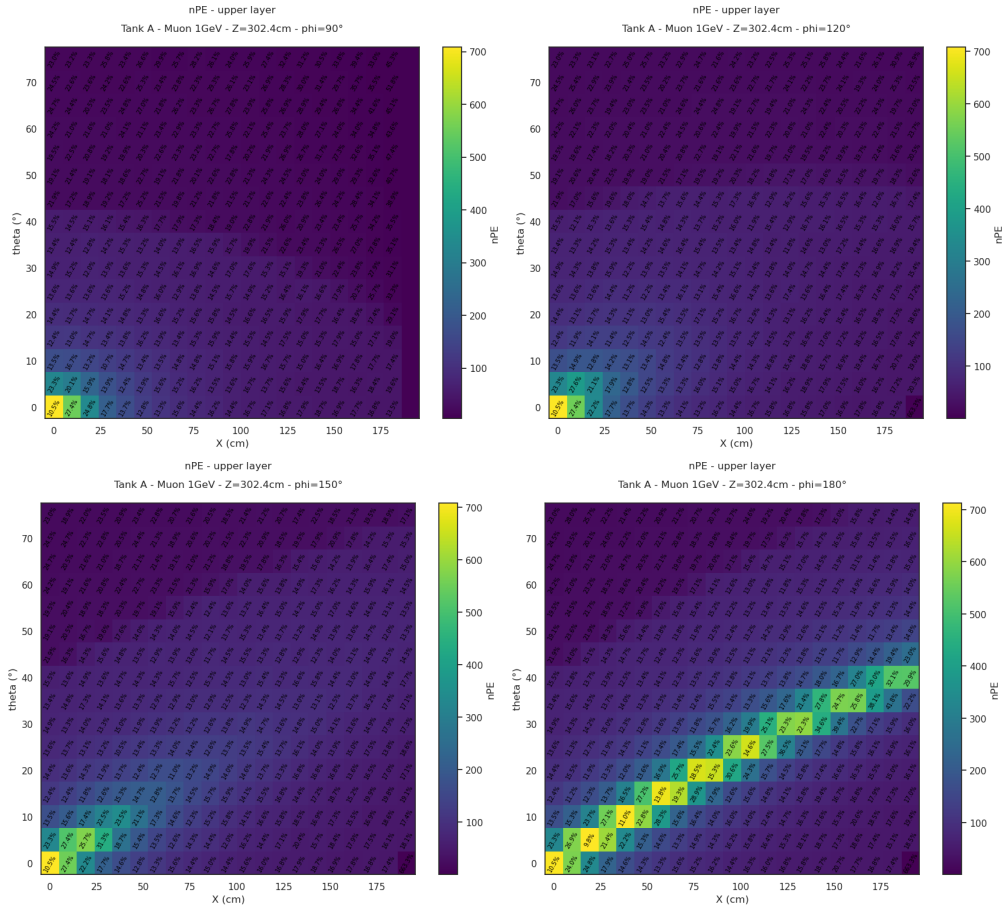

Figure 15: Number of photo-electrons detected in the upper layer for a 1 GeV muon (with fixed $\phi = 90°$, $\phi = 120°$, $\phi = 150°$ and $\phi = 180°$).

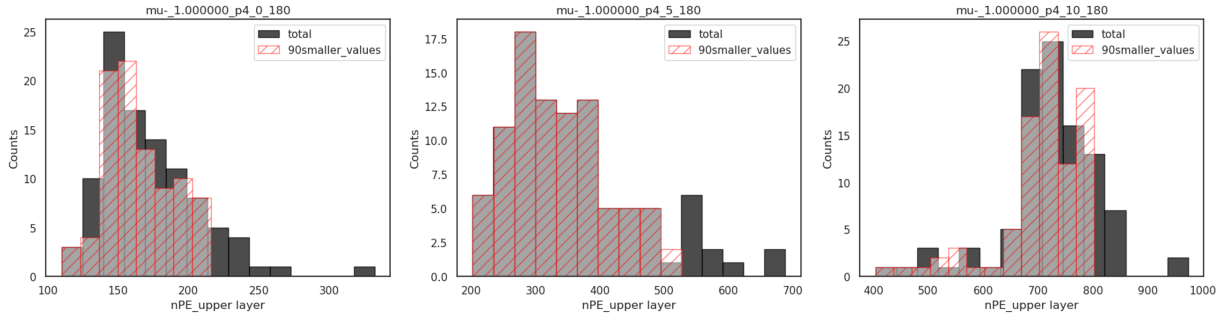

Figure 16: Histograms of nPE distributions for some 1 GeV muon configurations (upper layer).

A.9 Muons - 0.3 GeV

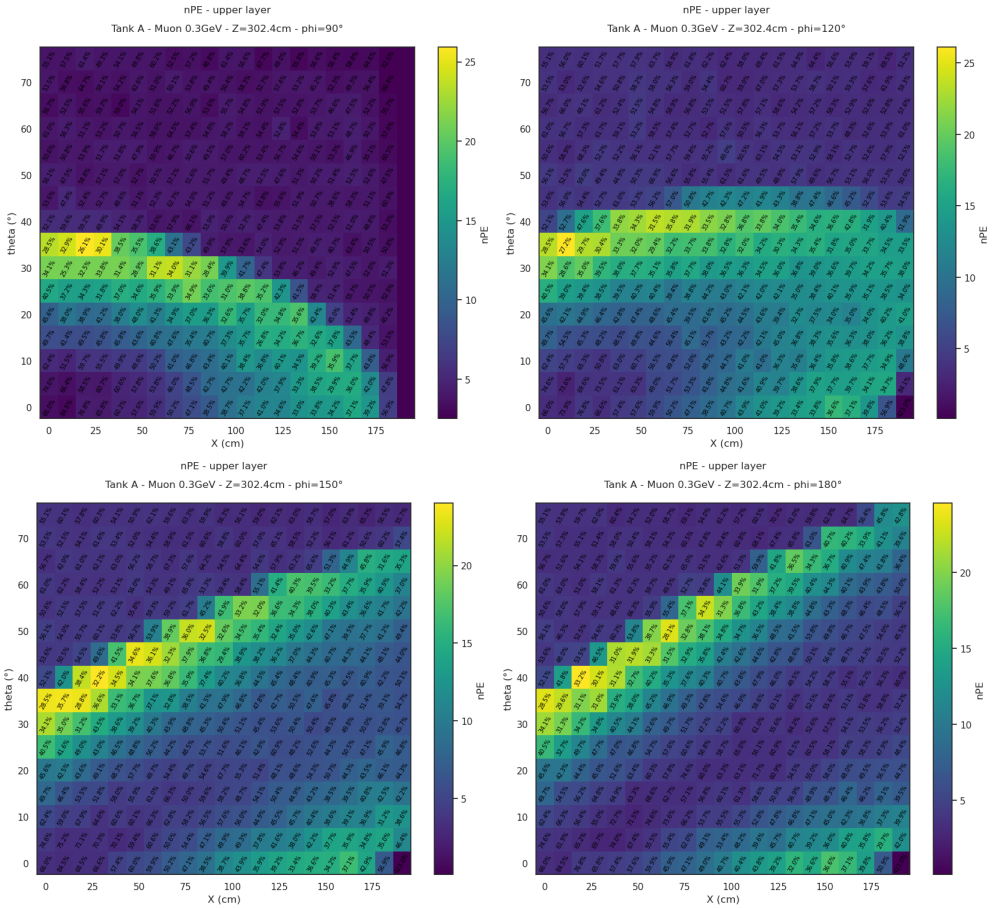

Figure 17: Number of photo-electrons detected in the upper layer for a 0.3 GeV muon (with fixed $\phi = 90°$, $\phi = 120°$, $\phi = 150°$ and $\phi = 180°$).

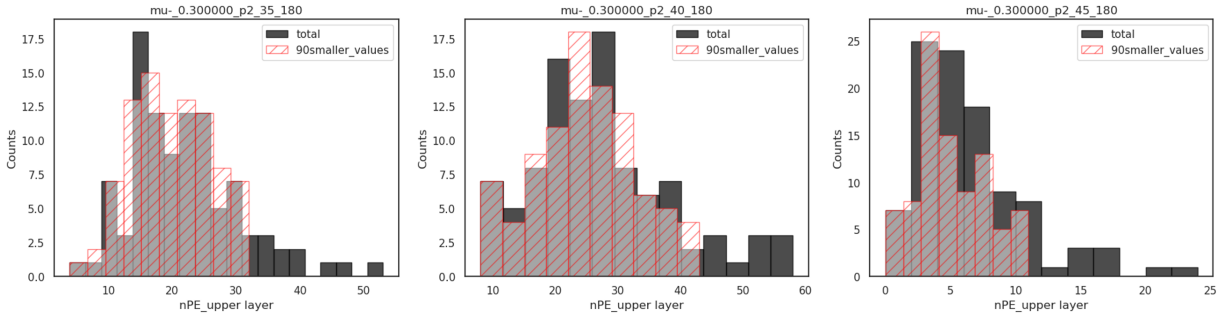

Figure 18: Histograms of nPE distributions for some 0.3 GeV muon configurations (upper layer).

B nPE - lower layer

B.1 Electrons - 3 GeV

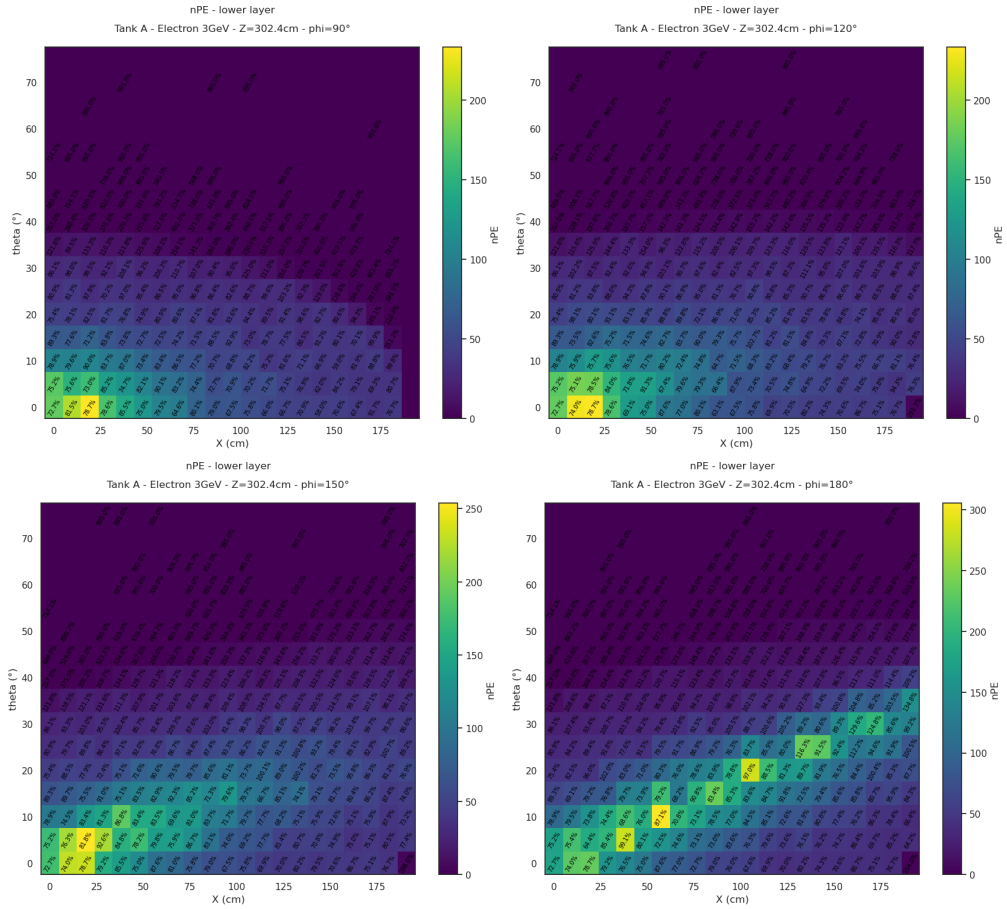

Figure 19: Number of photo-electrons detected in the lower layer for a 3 GeV electron (with fixed $\phi = 90°$, $\phi = 120°$, $\phi = 150°$ and $\phi = 180°$).

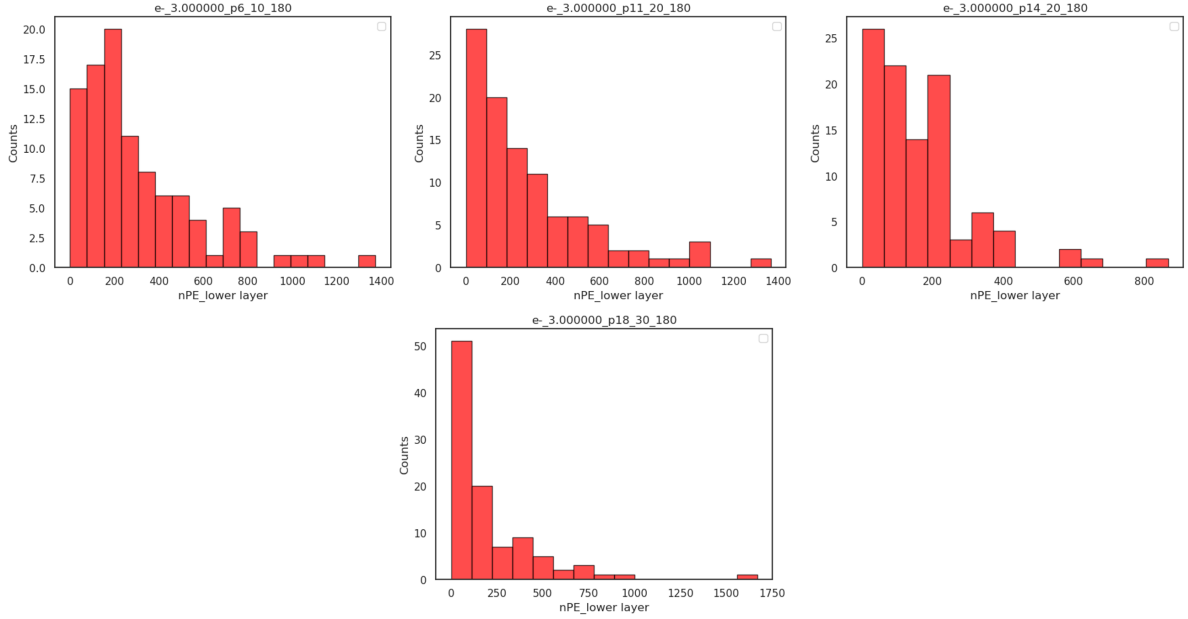

Figure 20: Histograms of nPE distributions for some 3 GeV electron configurations (lower layer).

B.2 Electrons - 0.3 GeV

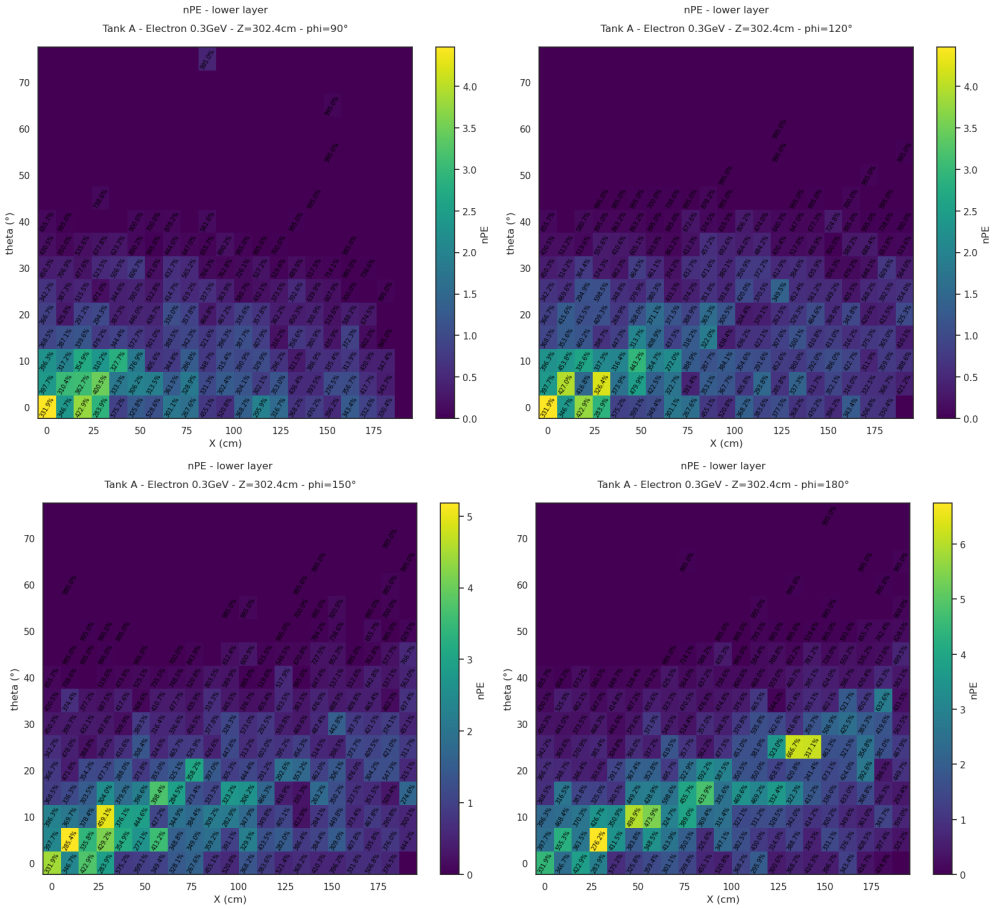

Figure 21: Number of photo-electrons detected in the lower layer for a 0.3 GeV electron (with fixed $\phi = 90°$, $\phi = 120°$, $\phi = 150°$ and $\phi = 180°$).

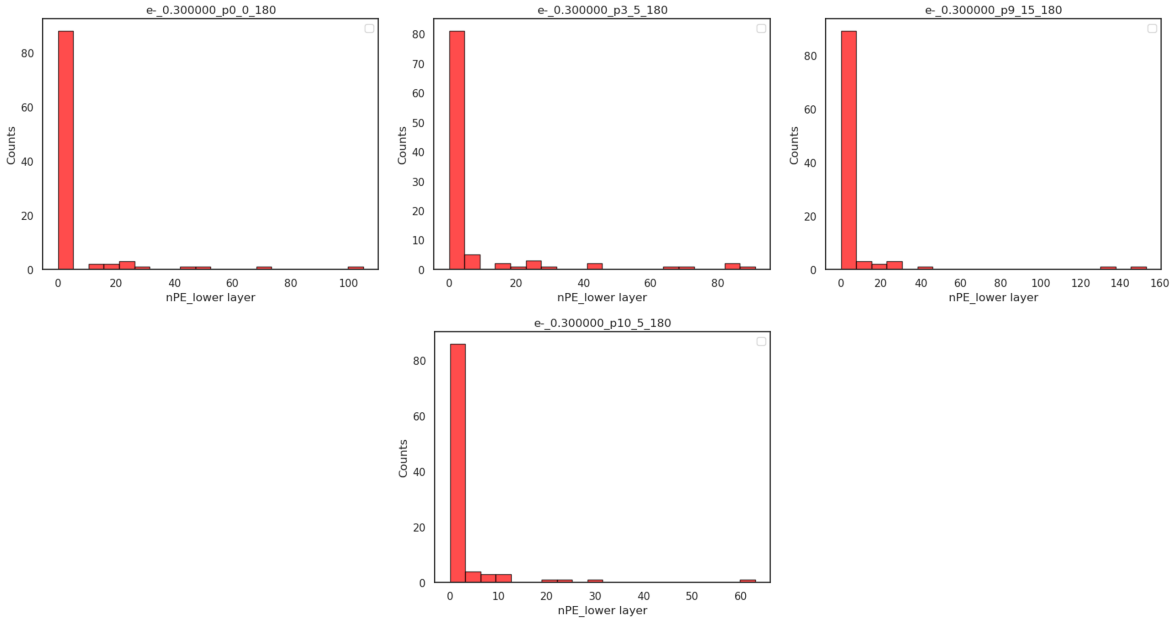

Figure 22: Histograms of nPE distributions for some 0.3 GeV electron configurations (lower layer).

B.3 Electrons - 0.03 GeV

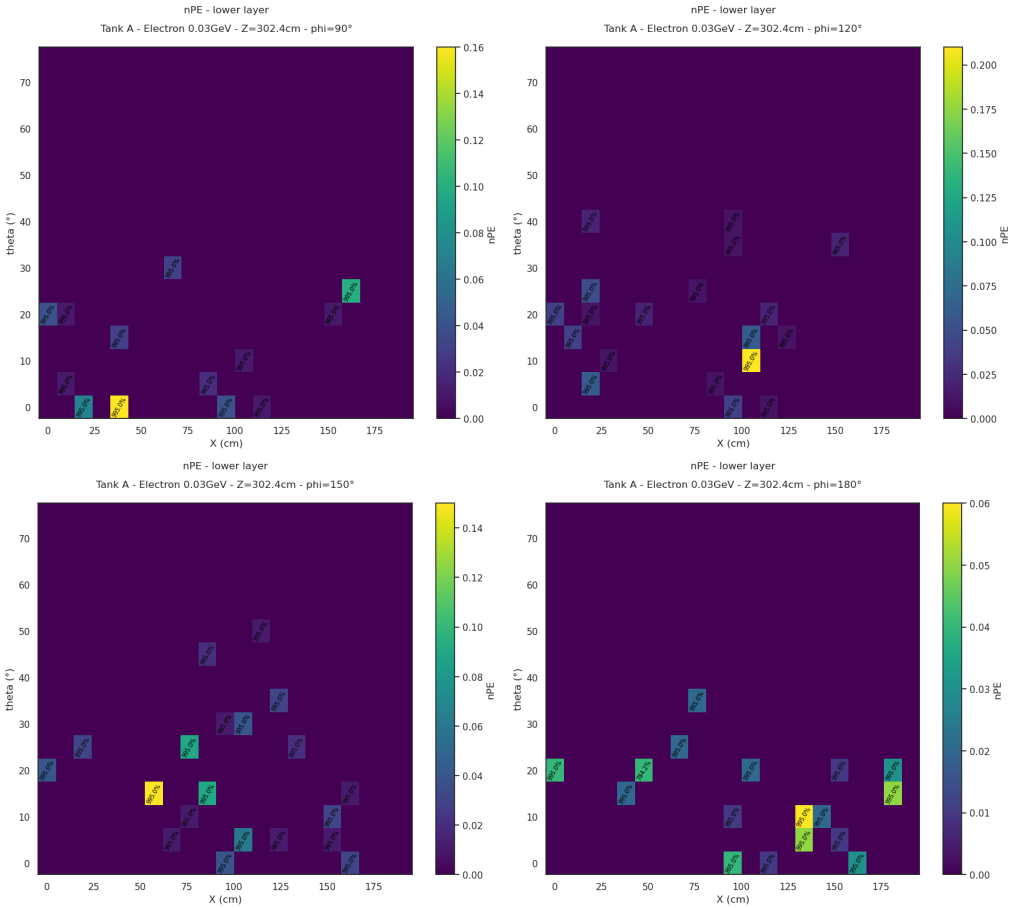

Figure 23: Number of photo-electrons detected in the lower layer for a 0.03 GeV electron (with fixed $\phi = 90°$, $\phi = 120°$, $\phi = 150°$ and $\phi = 180°$).

B.4 Muons - 200 GeV

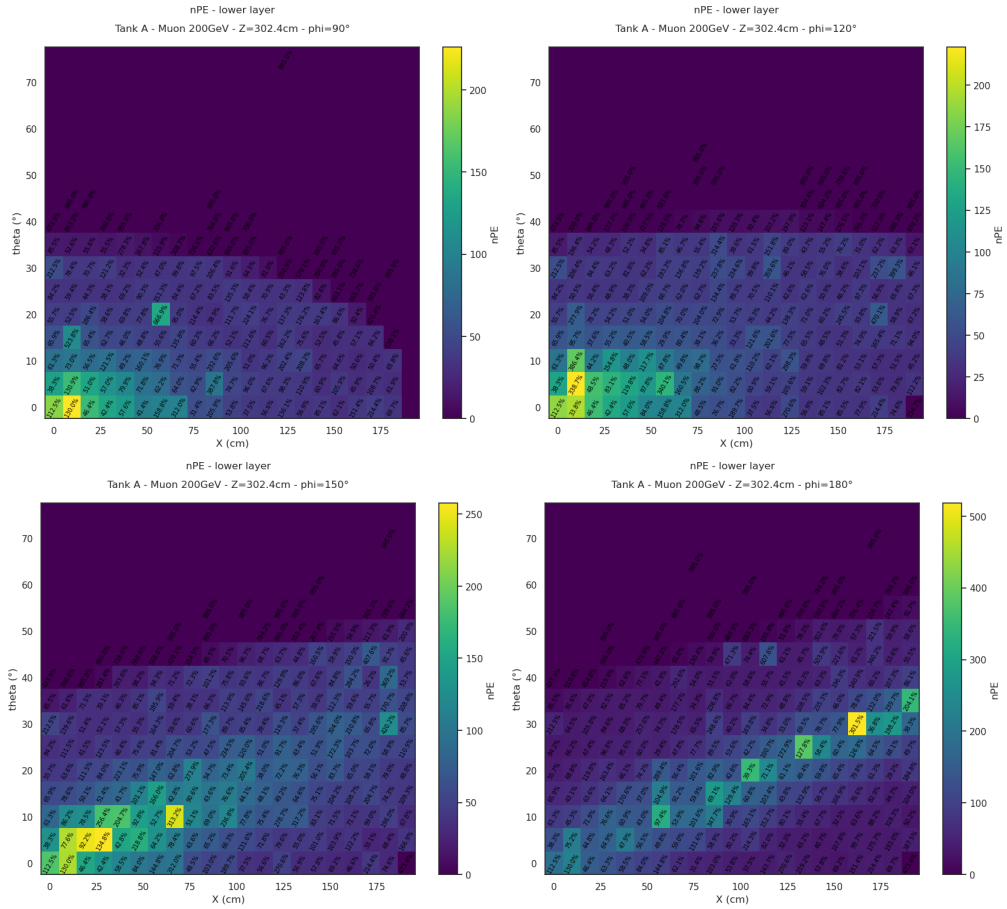

Figure 24: Number of photo-electrons detected in the lower layer for a 200 GeV muon (with fixed $\phi = 90°$, $\phi = 120°$, $\phi = 150°$ and $\phi = 180°$).

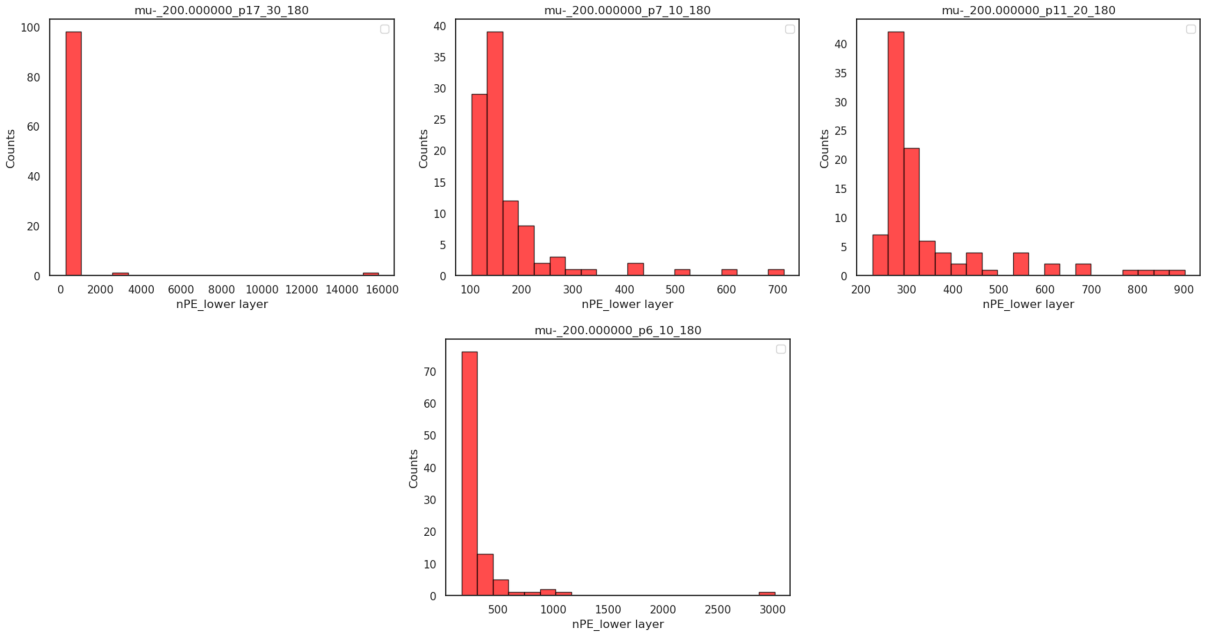

Figure 25: Histograms of nPE distributions for some 200 GeV muon configurations (lower layer).

B.5 Muons - 50 GeV

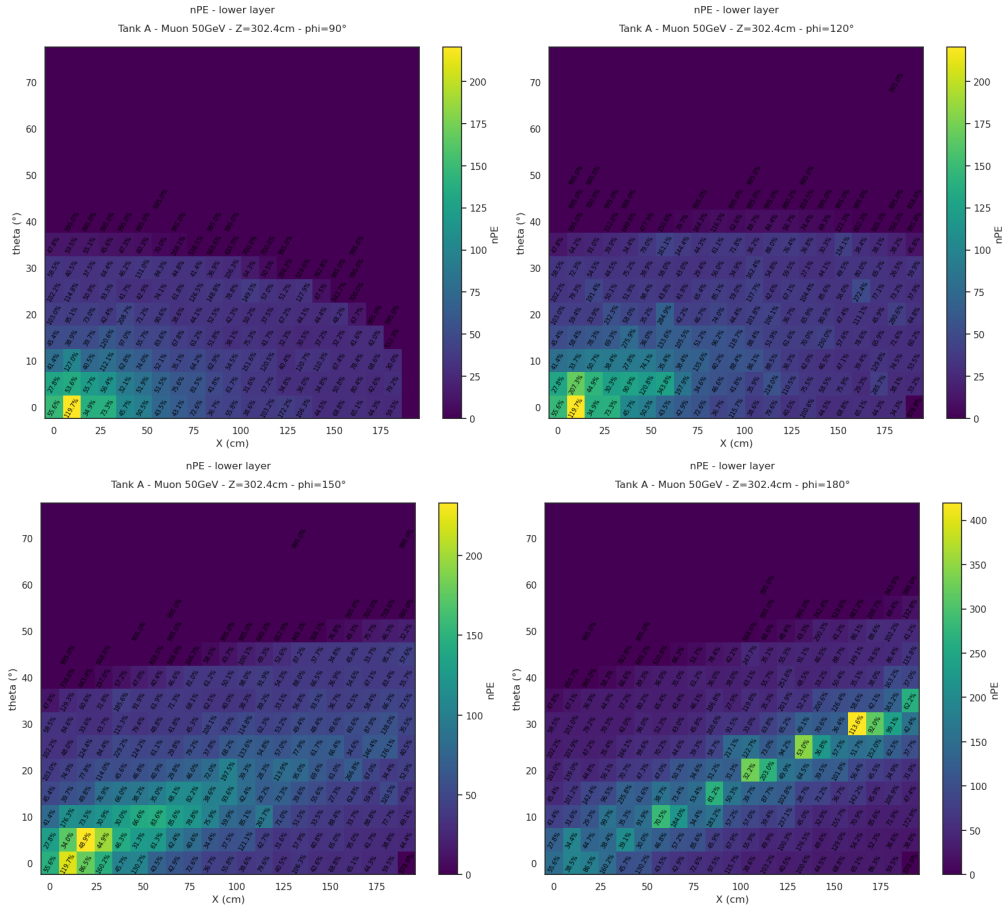

Figure 26: Number of photo-electrons detected in the lower layer for a 50 GeV muon (with fixed $\phi = 90°$, $\phi = 120°$, $\phi = 150°$ and $\phi = 180°$).

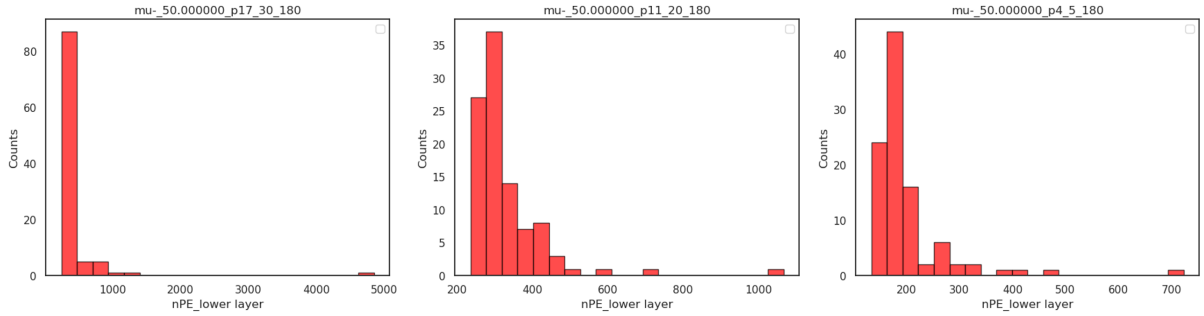

Figure 27: Histograms of nPE distributions for some 50 GeV muon configurations (lower layer).

B.6 Muons - 10 GeV

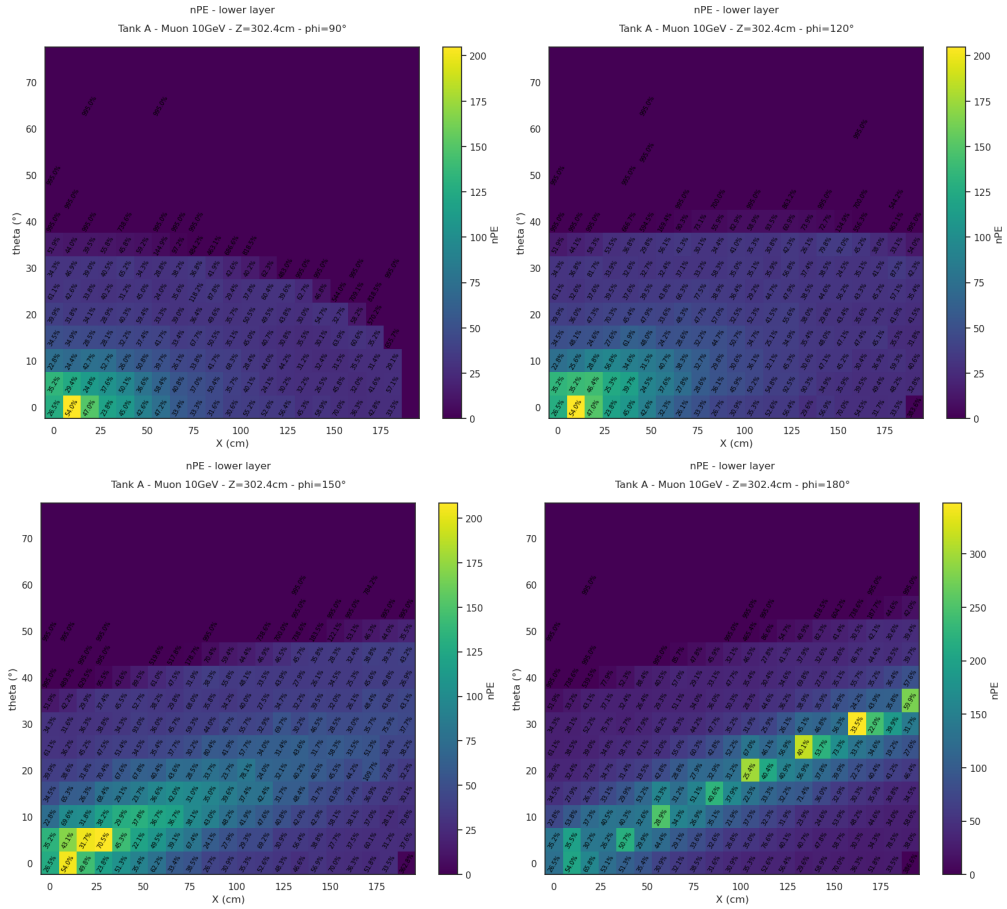

Figure 28: Number of photo-electrons detected in the lower layer for a 10 GeV muon (with fixed $\phi = 90°$, $\phi = 120°$, $\phi = 150°$ and $\phi = 180°$).

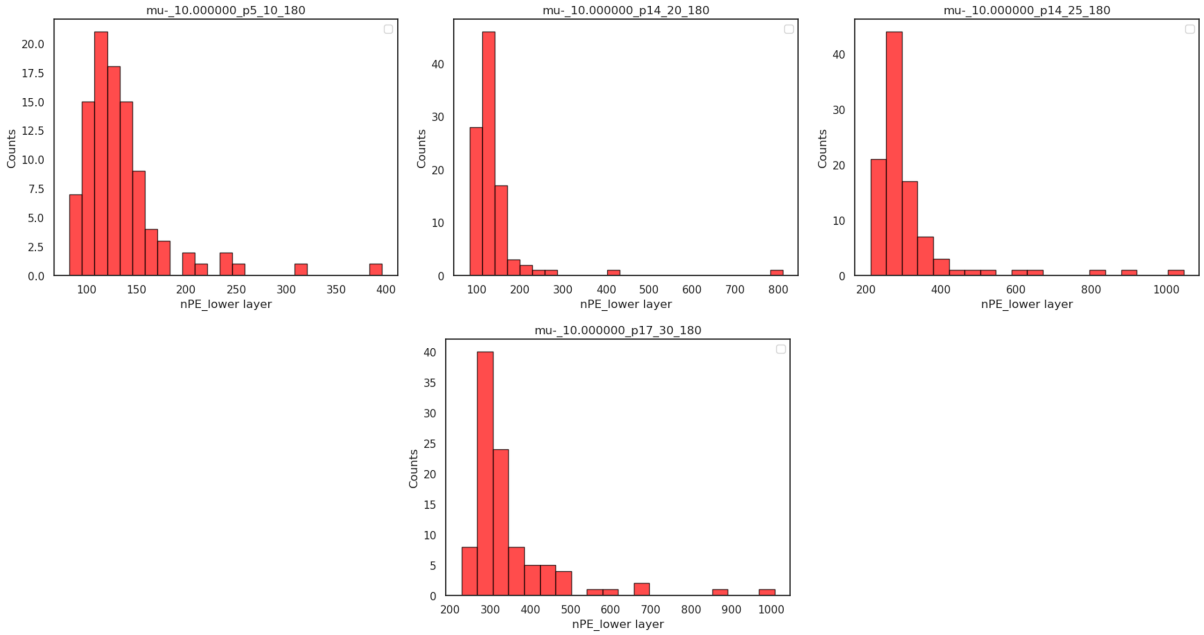

Figure 29: Histograms of nPE distributions for some 10 GeV muon configurations (lower layer).

B.7 Muons - 1 GeV

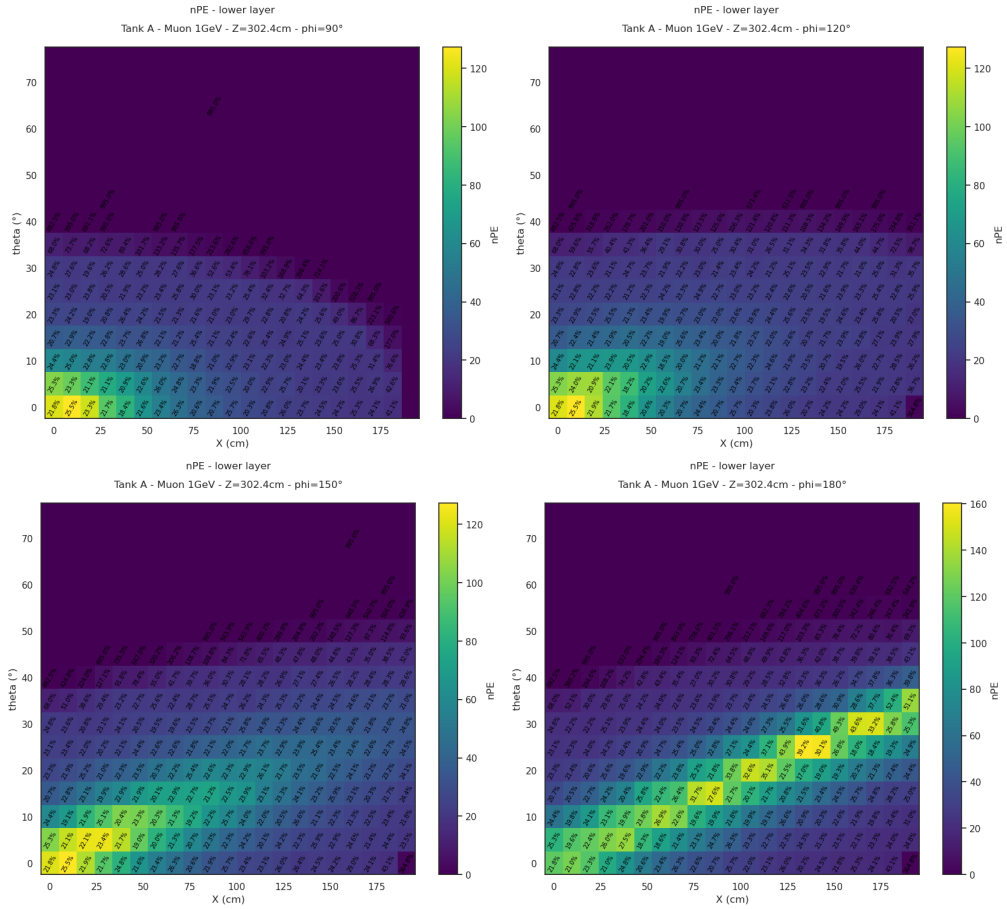

Figure 30: Number of photo-electrons detected in the lower layer for a 1 GeV muon (with fixed $\phi = 90°$, $\phi = 120°$, $\phi = 150°$ and $\phi = 180°$).

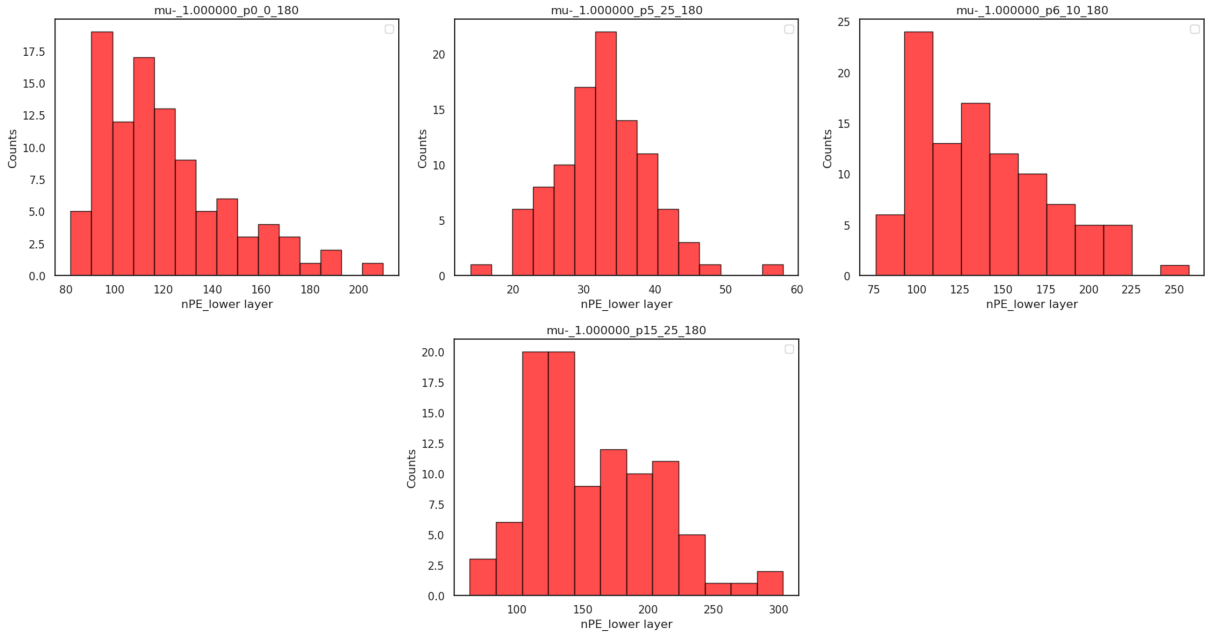

Figure 31: Histograms of nPE distributions for some 1 GeV muon configurations (lower layer).

B.8 Muons - 0.3 GeV

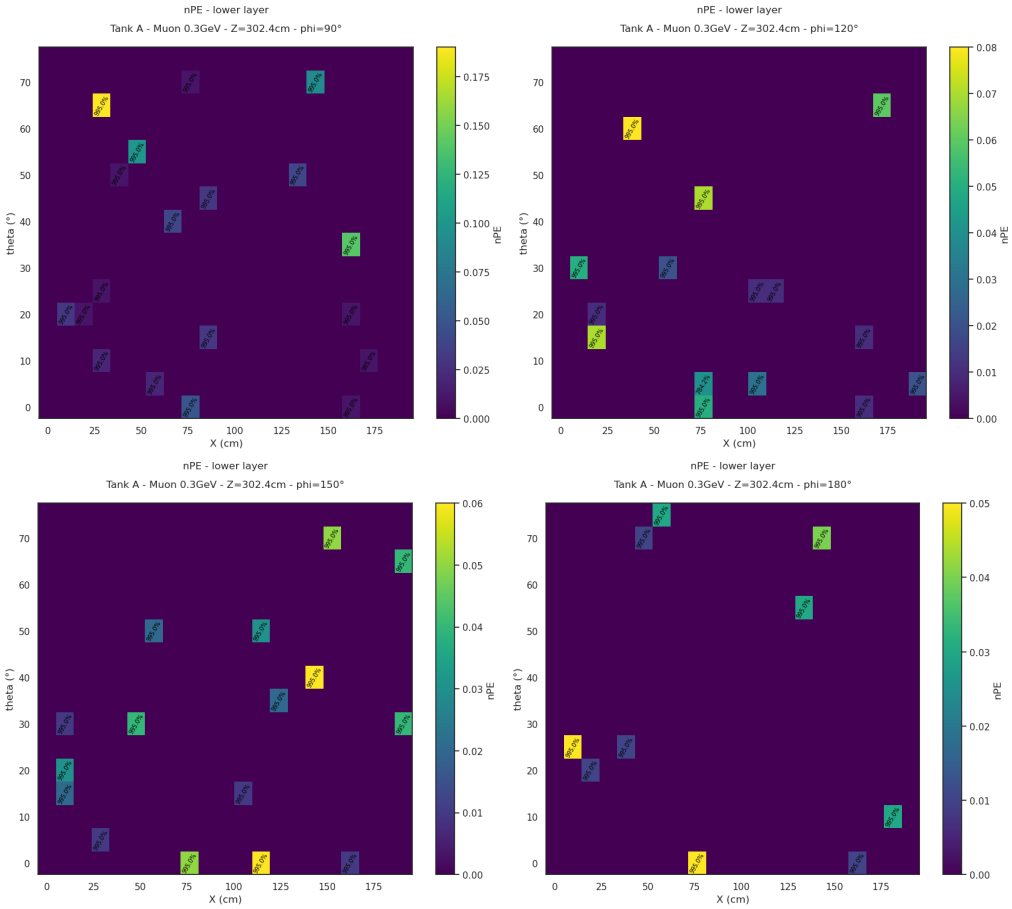

Figure 32: Number of photo-electrons detected in the lower layer for a 0.3 GeV muon (with fixed $\phi = 90°$, $\phi = 120°$, $\phi = 150°$ and $\phi = 180°$).

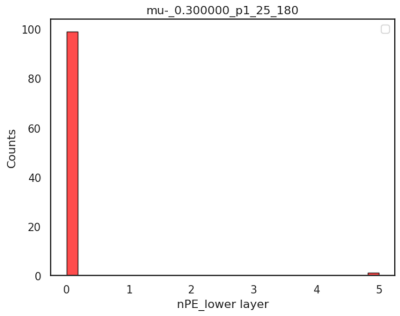

Figure 33: Histograms of nPE distributions for some 0.3 GeV muon configurations (lower layer).